# ANALYSIS OF THE TROPICAL TROPOPAUSE LAYER CIRRUS IN CALIPSO

# AND MLS DATA - A WATER PERSPECTIVE

A Thesis

by

TAO WANG

Submitted to the Office of Graduate Studies of
Texas A&M University
in partial fulfillment of the requirements for the degree of

MASTER OF SCIENCE

May 2011

Major Subject: Atmospheric Sciences

# ANALYSIS OF THE TROPICAL TROPOPAUSE LAYER CIRRUS IN CALIPSO

# AND MLS DATA - A WATER PERSPECTIVE

A Thesis

by

TAO WANG

Submitted to the Office of Graduate Studies of
Texas A&M University
in partial fulfillment of the requirements for the degree of

MASTER OF SCIENCE

Approved by:

Chair Committee,      Andrew E. Dessler
Committee Members,    Shaima L. Nasiri
                      Renyi Zhang
Head of Department,   Kenneth P. Bowman

May 2011

Major Subject: Atmospheric Sciences

**ABSTRACT**

Analysis of the Tropical Tropopause Layer Cirrus in CALIPSO

and MLS Data - A Water Perspective. (May 2011)

Tao Wang, B.S., Yunnan University

Chair of Advisory Committee: Dr. Andrew E. Dessler


Two mechanisms appear to be primarily responsible for the formation of cirrus clouds in Tropical Tropopause Layer (TTL): detrainment from deep convective anvils and in situ initiation. Here we propose to identify TTL cirrus clouds by analyzing water content measurements from the Cloud-Aerosol Lidar and Infrared Pathfinder Satellite Observations (CALIPSO) and Aura Microwave Limb Sounder (MLS). Using ice water content (IWC) and water vapor ($H_2O$) abundances we identify TTL cirrus clouds that contain too much ice to have been formed in situ — and therefore must be of convective origin. We use two methods to infer the maximum IWC available for cirrus formed in situ, serving as our threshold. Cirrus with IWC greater than this threshold are categorized as being of convective origin; cirrus with IWC below this threshold are ambiguous — they could either form in situ or still be of convective origin. Applying the thresholds from December 2008 to November 2009, we found three maxima in the occurrence of convective cirrus: equatorial Africa, western Pacific, and South America. Averaged over the entire tropics, we found that convective cirrus occur more frequently in boreal winter and less frequently in boreal summer, basically following a decreasing trend from DJF, MAM, SON, to JJA. At the tropopause (~375 K), at least 19.2% (4.6%) of TTL cirrus

were definitively of convective origin during boreal winter (summer). Sensitivity tests show that the thresholds derived at 390 K have the largest uncertainty. At lower levels, especially 375 K, our thresholds are robust.

# ACKNOWLEDGEMENTS

I thank my advisor, Dr. Andrew Dessler for offering me this opportunity to study and work on this interesting topic. I feel much appreciated for his support and encouragement during my work. Dr. Dessler's profound insight into global climate change inspires me greatly to keep exploring this cutting-edge issue. I thank him for supporting me to continue my education in Texas A&M University.

I thank my committee members, Dr. Shaima Nasiri and Dr. Renyi Zhang, for giving me a lot of valuable suggestions through my work. By working through some detailed questions brought by them, I learned even more. Great appreciation goes to Dr. Nasiri especially, for being extremely patient with me.

I also want to thank my group member, Abhishek Verma for his help and discussing scientific problems with me. Especially, I want to thank Alex Matus and Benjamin Cole for revising my thesis, correcting my English in such a specific manner.

Great appreciation goes to my parents and my brother for their endless love. I thank my wife, Jia for her unconditional love and support in every possible way. I feel so lucky to have her for my companion for the rest of my life.

# TABLE OF CONTENTS

## LIST OF TABLES

# LIST OF FIGURES

## 1.     INTRODUCTION

### 1.1     TTL cirrus and their radiative role

Cirrus are formed at higher altitudes (at lease above 8 km) where moisture is very limited, thus they tend to be thin.  Using ice as a classification indicator, cirrus referred in our analysis are high clouds that are completely composed of ice crystals.  Cirrus clouds are globally distributed, being present at all latitudes with no respect to land or ocean, or seasons of the year.  Cirrus generally cover 20% to 25% of the earth's surface [*Wang, et al.*, 1994; *Rossow and Schiffer*, 1999; *Sassen and Mace,* 2002], and up to more than 50% in the tropical western Pacific [*Prabhakara et al.*, 1993].   Despite their ubiquitous presence, cirrus clouds remain a substantial source of uncertainty in our understanding of the climate [*e.g., Liou, 1986*; *Lynch et al.*, 2002].

Of particular interests are cirrus clouds in the tropical tropopause layer (TTL), a transition layer that separates the troposphere and the stratosphere [*Highwood and Hoskins*, 1998; *Sherwood and Dessler*, 2000; *Fueglistaler et al.*, 2009] and therefore both tropospheric and stratospheric characteristics can be found within.  As shown in Figure 1.1, the bottom of the TTL is located at near 14.5 km (approximately 150 hPa or 355 K in potential temperature) [*Folkins et al.*, 1999; *Gettelman et al.*, 2004] and is usually defined as the level of zero net radiative heating (LZRH) [*Sherwood and Dessler*, 2000, 2001]. Below the bottom of the TTL, radiative cooling dominates, as air sinks back to the surface, driven by the tropical overturning Hadley or Walker circulation.  Above the

---

This thesis follows the style of *Journal of Geophysical Research – Atmosphere*.

bottom of the TTL, radiative heating dominates, as net radiative forcing changes from negative (cooling) to positive (heating) under clear-sky conditions. Driven in part by the stratospheric Brewer-Dobson circulation [*Brewer, 1949*], radiatively heated air eventually enters the stratosphere. The top of the TTL is the maximum height where overshooting convection occurs; this level is approximately 18-19 km in altitude, 70-80 hPa in pressure, or 410-420 K in potential temperature [*Alcala and Dessler*, 2002; *Fu et al.*, 2007]. The tropopause is located within the TTL around 17 km or 375 K, which is typically 1-2 km or about 20 K above the TTL bottom. More detailed discussion about the TTL can be found in the review by *Fueglistaler et al.* [2009].
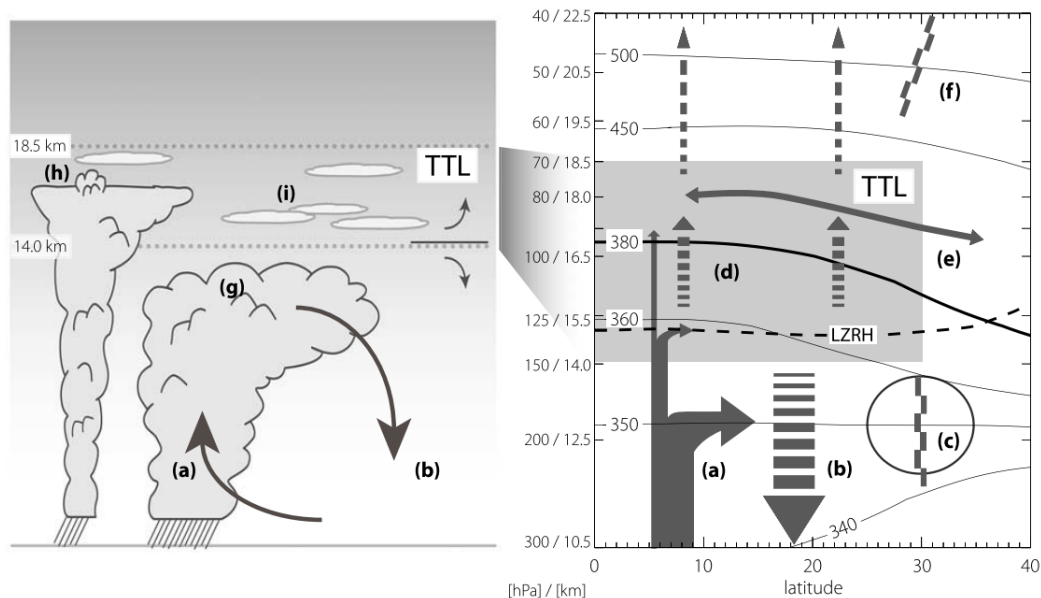


**Figure 1.1.** Schematic show of the TTL. Letters **a** and **b** indicate deep convection and radiative cooling; letter **d** indicates radiative heating; letters **g** and **i** indicates deep convective clouds and thin cirrus clouds (often formed in situ). Adapted from *Fueglistaler et al.* [2009].

TTL cirrus clouds occur frequently [e.g., *Wang et al., 1996*]. They can extend several hundred kilometers horizontally [*McFarquhar et al.*, 2000*; Winker and Trepte*, 1998] and persist over several hours or even days [*McFarquhar et al.,* 2000; *Dinh et al.*, 2010]. Given their extensive spatial and temporal attributes, it is widely accepted that TTL cirrus clouds play a significant role in the radiative budget of the TTL by regulating both longwave (infrared) and shortwave (solar) radiation [*McFarquhar et al.*, 2000] and the transportation of trace constituents, particularly water vapor, into the stratosphere [*Gettelman et al.*, 2002; *Dessler and Minschwaner*, 2007]. A detailed cirrus model study by *Jensen et al*. [1996] estimated that the absorption of infrared radiation by thin cirrus clouds in the tropical tropopause might increase heating rates by several Kelvin per day. Another study of a chemistry-radiation-dynamics model by *Rosenfield et al.* [1998] showed that subvisible cirrus formation increases radiative heating by 0.1-0.2 K/day by absorbing outgoing longwave radiation from the lower troposphere, which may increase the average temperature of the TTL by 1 to 2 K. TTL warming increases water vapor transport into the lower stratosphere. Since water vapor in the stratosphere is largely determined by transport through the tropopause [*Brewer*, 1949; *Solomon et al.*, 2010], cirrus formation eventually increases water vapor abundance in the lower stratosphere. Many research has shown that water vapor in the stratosphere has been increasing [*Oldmans and Hofmann,* 1995; *Evans et al.*, 1998; *Rosenlof et al.*, 2001; *Hurst et al.,* 2011], which cools the stratosphere but warms the troposphere [*Forster and Shine, 1999; Smith et al., 2001*].

Numerous studies have assessed the frequency of occurrence and distribution of tropical cirrus clouds. *Eguchi et al.* [2007] reported that cirrus of at least 14 km height

occurs 30% of the time in the tropics. Compared with other tropical regions, they are less frequent over the tropical eastern Pacific. *Haladay and Stephens* [2009], using observation from the Cloud-Aerosol Lidar and Infrared Pathfinder satellite observation (CALIPSO), revealed that cirrus with cloud tops of 13 km to 18 km cover 30% of tropical region between 20$^o$ N/S. Another study by *Massie et al.* [2010] observed the seasonal variations of occurrence of tropical cirrus from measurements of CALIPSO and High Resolution Dynamics Limb Sounder (HIRDLS), and concluded that frequency is highest during boreal winter and lowest during boreal summer.

## 1.2    TTL cirrus formation

Understanding the mechanisms responsible for the formation of TTL cirrus is an important step in predicting cirrus occurrence in radiation and climate models. Previous studies have suggested that two mechanisms appear to be primarily responsible for the formation of cirrus clouds in the TTL: in situ initiation and convective formation.

The in situ formation can be driven by either large scale vertical uplifting or temperature perturbations from Kelvin or gravity waves. *Jensen et al.* [1996], using a detailed cirrus model, estimated that in situ ice nucleation initiated from synoptic-scale uplift cooling of a humid layer or from shear turbulent mixing may result in the formation of thin cirrus clouds. *Pfister et al*. [2001] suggested the same formation mechanism based on an analysis of temperatures along back trajectories and pointed out that large-scale uplift could also occur on the mesoscale. This uplift cooling could be driven by flow over large-scale convective systems or above stratiform regions [*Churchill and Houze*, 1990]; it can also be driven by momentum transport initiated from convectively

initiated Rossby waves in the Intertropical Convergence Zone (ITCZ) regions [*Boehm and Lee*, 2003].

Another in situ formation process is the negative temperature (cold) anomalies driven by equatorial Kelvin waves, which lead to regular formation of extremely thin cirrus clouds [*Boehm and Verlinde*, 2000; *Immler et al.*, 2008; *Fujiwara et al.*, 2009]. Results show that cold anomalies with downward propagation of Kelvin waves from the lower stratosphere into the TTL provide favorable conditions in the TTL for adiabatic cooling of air parcels. Cooling is followed by ice nucleation and dehydration, forming thin cirrus clouds. Those cirrus are usually observed detached from convection (see the isolated cirrus labeled in Figure 1.2).
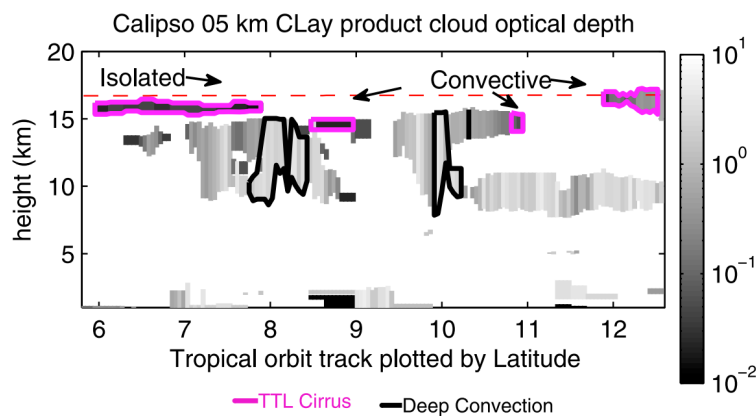
**Figure 1.2.** An example of cirrus clouds from CALIPSO 05 km Cloud Layer (CLay) product. In this figure, cirrus is outlined in pink; black outlines deep convection. The isolated cirrus is most likely formed in situ; while the convective cirrus formed from convective anvil blow-off. Gray scale colorbar indicates cloud layer optical depth. Adapted from *Riihimaki and McFarlane* [2010].

This is not the case for cirrus clouds of convective formation. Recent detrainment from deep convective anvils that penetrate into the TTL could inject large amount of ice crystals into ambient air, forming physically and optically thick cirrus [*Pfister et al.*, 2001; *Comstock and Jakob*, 2004] (see Figure 1.2 the cirrus labeled as convective). But the story is not finished. After a long dissipation time, thick cirrus gradually thin out and advect away (detached) from the original convection region, with the remnant ice crystals still persist, existing as thin cirrus clouds [*Jensen et al.*, 1996; *Mace et al.*, 2006]. The dissipation occurs either in supersaturated air in which ice crystals grow by deposition and then fall out, or in subsaturated air where ice particles sublimate. It may also occur because of the horizontal wind shear that thins out the layer when cirrus persists for a longer time. In our study, we focus mostly on the cirrus of convective formation.

## 1.3    Connection between TTL cirrus and deep convection

Numerous studies have assessed the connection between TTL cirrus and deep convection. To summarize, those works usually start from three perspectives.

First, some works found that TTL cirrus generally occur over convectively active regions such as the warm pool (western Pacific), or regions of low outgoing longwave radiation (OLR), therefore they thought that those clouds must have strong relation with deep convection. Using *Nimbus-4* Infrared Interferometer Spectrometer (IRIS) data, *Prabhakara et al.* [1988] deduced that thin cirrus clouds were 100–200 km away from the center of high-altitude cold clouds, and hence were associated with convectively active regions such as the ITCZ and the Bay of Bengal. In a later study [*Prabhakara et al.*, 1993], they found that IRIS observed thin cirrus clouds exist near the tropopause

more than 50% of the time in warm pool regions. *Wang et al.* [1996] estimated the coverage of tropical subvisual cirrus to be 45% in the zonal mean and 70% in the annual mean over the western Pacific, based on aerosol extinction data from the Stratospheric Aerosol and Gas Experiment (SAGE) II. *Winker and Trepte* [1998] observed laminar clouds from the Lidar In-space Technology Experiment (LITE) to show that cirrus in the tropical western Pacific may exist both detached from and closely associated with deep convective clouds. *Massie et al.* [2002] established statistical and geographical relationships between subvisual cirrus clouds, based on aerosol extinction data from the Halogen Occultation Experiment (HALOE), and deep convection, based on outgoing longwave (OLR) radiation data from the Climate Diagnostics Center (CDC). They found that occurrence rates of cirrus are larger over regions of deep convection than away from deep convection. At 121 hPa, they found that cirrus is observed 80% of the time when OLR is less than 150 W/m$^2$. *Dessler et al.* [2006] analyzed the distribution of thin cirrus in the tropics using measurements from the GLAS (Geoscience Laser Altimeter System), on board the Ice, Cloud, and land Elevation Satellite (ICESat). By comparing cirrus location with OLR, they found general consistency between cirrus frequency maxima and OLR minima, which means cirrus occurrence is strongly correlated with convection. Using the same datasets, *Eguchi et al.* [2007] observed more than 70% of cirrus occurs over regions of tropical convection and therefore they concluded that those clouds are closely related to convection anvil outflow.

Second, many works on model simulations found that some cirrus could be traced back to convection. *Massie et al.* [2002] used a five-day back trajectory simulation and found that nearly half of the HALOE cirrus observations in the maritime continent can be

traced back to deep convective blow-off. *Mace et al.* [2006], combined millimeter cloud radar (MMCR) observations of cirrus clouds and GMS (Geosynchronous Meteorological Satellite) satellite-derived back trajectories, found that 47% of cirrus observed over a western Pacific island, Manus, can be traced back to deep convective activity within 12 hours. From the same analysis, they found that 16% of cirrus observed at a central Pacific island, Nauru, can also be traced back to deep convection.

Finally, many works found that some cirrus clouds are collocated with deep convective clouds, and they suspect, therefore, that those clouds should be related to deep convection. *McFarquhar et al.* [2000], comparing subvisible cirrus observed by SAGE II (the Stratospheric Aerosol and Gas Experiment) with ISCCP (International Satellite Cloud and Climatology Project) derived deep convective clouds, found at least 28% of them were collocated with deep convective clouds. *Sassen et al.* [2009] studied the occurrence and diurnal variations of tropical cirrus and deep convective clouds from joint observations of space-based lidar and radar, they found that cirrus and deep convection prevail/absent in the same pattern, then they concluded that cirrus cloud formation in the tropics is generally tied to the direct and/or indirect effects of deep convection. More recently, *Riihimaki et al.* [2010], using CALIPSO lidar measurements from July 2006 through June 2009 data, revealed that 36% of thin cirrus clouds were connected to convection because they are directly attached to optically thick clouds with tops greater than 10 km – their definition of convective clouds.

**1.4    Motivation and basic idea**

Much of the above works studied the connection between cirrus and convection from the comparison with either typical deep convective regions or deep convective clouds. Typically they tried to answer two questions: 1) whether the occurrence of the TTL cirrus are related to deep convection; 2) if they are, then how many of them. This brings up the motivation of our work. We are wondering:

• Just start from cirrus observations, is there a general way to determine if TTL cirrus definitely originate from convection?

• If there is a way, then what fraction of the TTL cirrus clouds originates from deep convection?

• What is the distribution pattern of TTL cirrus clouds that are of convective origin? Does it vary seasonally?

• Can simple models reproduce the observations?

• What role does supersaturation and convection play in determining the occurrence patterns of TTL cirrus?

Instead of comparing with deep convective clouds (regions) or running model simulations, in our work, we will introduce a general way to identify those TTL cirrus that were definitively originated from convection by analyzing the water content within cirrus. This idea is inspired by the TTL cirrus formation mechanisms.

For in situ formation of cirrus clouds (hereafter *in situ cirrus*), ice crystals nucleate through adiabatic cooling. For example, we have limited amount of water molecules floating in the TTL air (Figure 1.3 a). When this parcel is being lifted up, through in situ adiabatic cooling, the formation of ice particles depletes water in the gas

phase (vapor) and enhances water in the solid phase (ice). From the water content perspective, the final ice water content (IWC) within cirrus clouds, therefore, does not exceed the initial water vapor ($H_2O$) abundance before nucleation (this is true even if precipitation occurs). Therefore, the amount of ice within is situ cirrus is limited by how much $H_2O$ is available in the ambient air before condensation. Since $H_2O$ abundance in the TTL is very low due to extremely low temperatures, in situ cirrus clouds are expected to have relatively lower IWC.

It is different for the convective formation of cirrus (hereafter *convective cirrus*). We understand that convection comes from the boundary layer, where there are tons of water molecules (Figure 1.3 b). The deep convective clouds take those water molecules up to form lots of ice particles. In convective formation, most of the ice crystals within cirrus originate from anvil blow-off. For cirrus initiated in this way, they could have more ice due to injection from anvils, which makes them thicker geometrically and optically. Therefore, the amount of ice within convective cirrus is not limited by how much $H_2O$ is available in the upper ambient air.
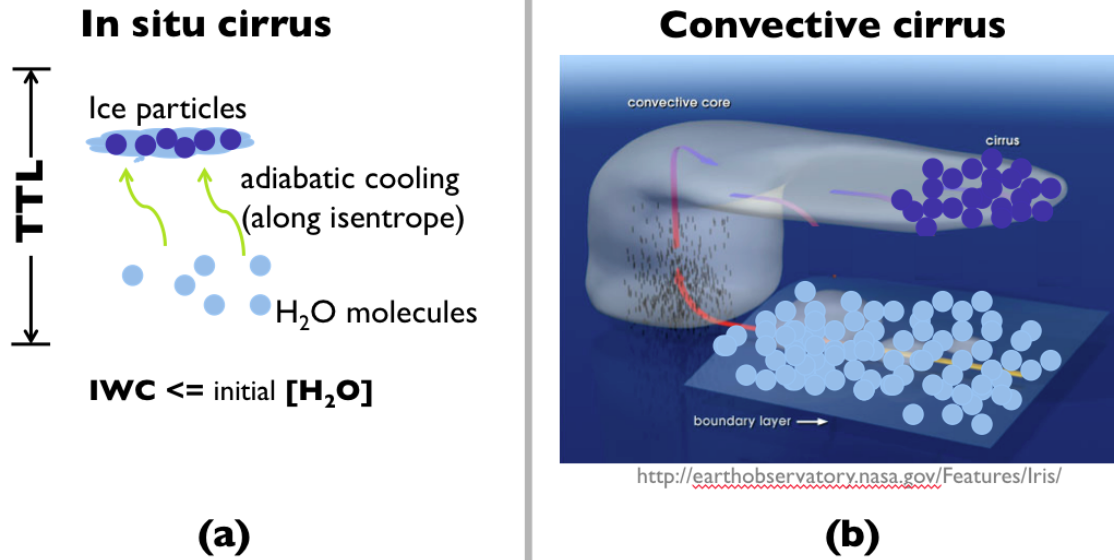
**Figure 1.3.** Schematic show of cirrus formed in situ (a) and from convection blow-off (b, adapted from NASA online sources at http://earthobservevatory.nasa.gov/Features/Iris/). The light blue dots indicate water molecules; dark blue dots indicate ice particles formed from nucleation of water vapor.

The above explanation from the water perspective serves as a cut-in point for our research: TTL cirrus containing more IWC than is available in gas phase in the ambient air must be of convective origin. Thus, by finding how much $H_2O$ is available in the ambient TTL air, we know how much ice can be found within in situ cirrus. Beyond this amount of ice, cirrus must come from convection. We therefore need to determine an IWC threshold whereby clouds that exceed that threshold were formed from convection. This threshold is determined by the $H_2O$ abundances in the ambient air. Further details on finding this crucial IWC threshold can be found in Section 3. To summarize, water content (both solid phase and vapor phase) within cirrus clouds are crucial factors for identifying cirrus clouds initiated from convection.

## 1.5    A-Train and thesis structure

The launch of the Afternoon satellite constellation (A-Train) in 2006 has provided an unprecedented wealth of measurements of cirrus clouds.  We choose satellite measurements not only because they provide water content measurements of cirrus clouds, but also because their wide spatial and temporal coverage.  We study the TTL cirrus clouds by analyzing the water content of measurements from the Cloud-Aerosol Lidar and Infrared Pathfinder Satellite Observations (CALIPSO) and Aura Microwave Limb Sounder (MLS).  CloudSat measurements are also investigated in this study because they provide water content products as well.  As members of the A-Train, they follow sun-synchronous orbits, passing the equator at approximately 1:30 pm and 1:30 am local solar time, observing the atmosphere comprehensively on a nearly global scale. This allows us to study cirrus clouds on a global scale with continuous observations.

This study will be the first time that TTL cirrus clouds are being explored from joint observations of CALIPSO and MLS from a water content perspective.  An overview of the TTL cirrus formation mechanisms and identification methods, as well as their seasonal and diurnal distribution patterns from December 2008 to November 2009, will be presented in the remaining parts of this thesis.

The remainder of this thesis is organized in the following manner. Section 2 describes the datasets their usage.  Section 3 outlines the methodology of the identification, which includes two methods based on CALIPSO and MLS observations to infer the IWC thresholds.  Section 4 presents the distribution patterns of both the total cirrus and the convectively originated cirrus clouds, including their seasonal variations.

A discussion of the robustness of thresholds we obtained is also included in this section.

The final conclusion and discussion are provided in Section 5.

## 2.   DATASETS AND THEIR USAGE

Aircraft-based in situ measurements and ground- and satellite-based remote sensing measurements have provided invaluable datasets depicting the behavior and microphysical properties of cirrus clouds (e.g., *Heymsfield and Jahnsen*, 1974; *Wang et al.*, 1996; *Winker and Trepte*, 1998; *McFarquhar et al.*, 2000; *Comstock et al.*, 2002; *Dessler et al.*, 2006; *Sassen et al.*, 2009).

Aircraft-based in situ observations, with high temporal and spatial resolution, provide the most direct measurements of cirrus clouds.  However, in situ measurements are very much constricted not only due to their limited temporal and spatial coverage, but also because direct measurements are even more difficult to conduct, especially for those tropical cirrus that exist at very high altitudes and extremely cold temperatures.  Their limited temporal and spatial coverage restrict their usefulness.  The spatial and temporal limitation is also the case with ground-based field campaigns.  Those limitations make it impossible to develop a statistically significant knowledge of the unique characteristics of TTL cirrus clouds.  Therefore, only satellite-based remote sensing provides sufficient coverage for our analysis.

The measurements we will use in this study come from the A-Train satellite constellation.  Currently, the A-Train consists of four NASA missions: Aqua (launched in 2002), Aura (launched in 2004), the Cloud-Aerosol Lidar and Infrared Pathfinder Satellite Observations (CALIPSO) and CloudSat (both launched together in 2006).  In addition, one French mission called Polarization and Anisotropy of Reflectances for Atmospheric Science coupled with Observations from a Lidar (PARASOL, launched in

2004) is also included, although it has now fallen out of the A-train due to fuel constraints. The satellites fly at an altitude of 705 km in a sun-synchronous polar orbit with an equator crossing time of about 1:30 p.m. and 1:30 a.m. local solar time (see Figure 2.1).
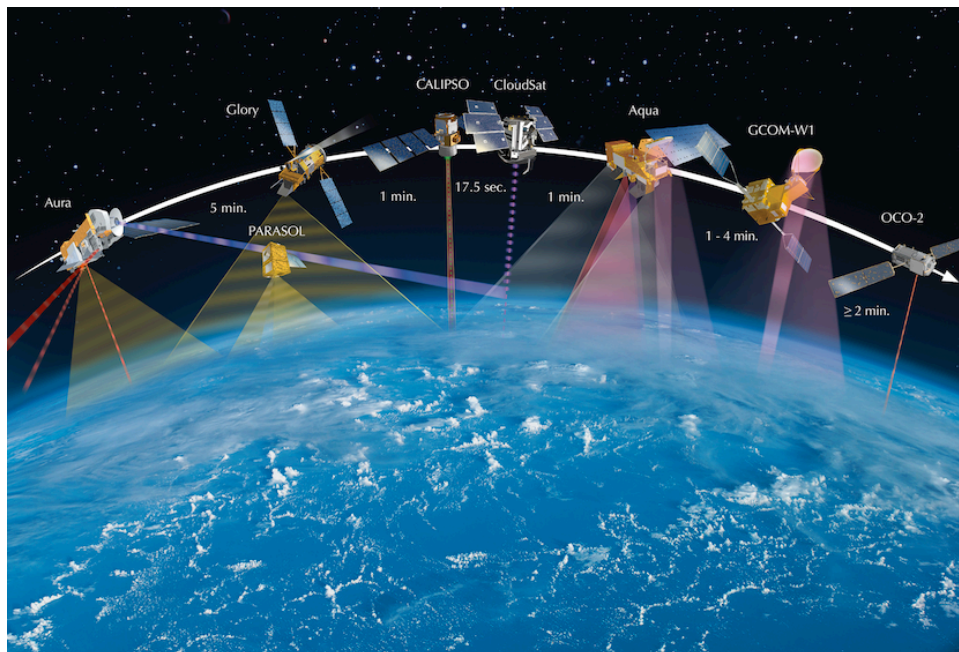


**Figure 2.1**. The Afternoon Constellation or A-Train. Two additional NASA Missions, Glory and the second Orbiting Carbon Observatory (OCO-2), as well as the Japanese Global Change Observation Mission-Water (GCOM-W1) mission will join the A-Train when they launch. (From http://atrain.nasa.gov/intro.php).

The A-Train provides a unique opportunity to observe and cross validate cloud observations made from specifically designed instruments. The high-quality data from A-Train will improve our understanding of atmospheric hydrological processes, atmospheric transport, and clouds' role in Earth's present and future climate.

As mentioned in Section 1, comparisons between the ice water content (IWC) of clouds and water vapor ($H_2O$) abundances in ambient air allow us to identify cirrus of convective origin. Thus, accurate measurements or retrievals of these quantities will be the crucial factor for our study. In this section, we compare IWC retrieved from different satellites to provide insight into the datasets and their usage. Then, there will be a brief introduction to our analysis of estimating $H_2O$ abundance.

## 2.1    IWC comparison

Currently, three satellites in the A-Train provide measurements of IWC. They are the CloudSat Cloud Profiling Radar (CPR), the Microwave Limb Sounder (MLS) onboard the Aura, and the Cloud-Aerosol lidar with Orthogonal Polarization (CALIOP) onboard the CALIPSO. We will next compare the IWC measured by different active instruments.

### 2.1.1   IWC from CloudSat

The CloudSat CPR is a 94-GHz nadir-looking radar, providing cloud location and classification, cloud ice and liquid water content, and cloud radiative fluxes and heating rates, etc. [*Stephens et al.*, 2002]. CloudSat derives IWC by using the IWC-Z-T relationship described by *Protat et al.* [2007]. The temperature (T) is provided by the auxiliary CloudSat product ECMWF-AUX, which comes from European Centre for Medium-Range Weather Forecasts (ECMWF) reanalysis. The IWC-Z-T algorithm is applied to CloudSat Z and EMWF-AUX T at each radar range bin to produce IWC. CloudSat provides IWC at 125 range bins with ~240 m intervals from the surface to

about 28 km in altitude. The CPR footprint and result IWC profile is 1.7 km along track by 1.4 km across track.

There are two standard IWC products in the latest release 04 (R04) of CloudSat datasets: the radar-only (RO) Cloud Water Content (CWC) product (2B-CWC-RO) and the radar-visible optical depth (RVOD) product (2B-CWC-RVOD). The 2B-CWC-RVOD combines CloudSat reflectivity and Moderate Resolution Imaging Spectroradiometer (MODIS, onboard the Aqua satellite of the A-Train) visible optical depth estimates to constrain the cloud retrievals and produce accurate results. When optical depth retrievals are unavailable, the radar-only retrieval, the 2B-CWC-RO, is used. The 2B-CWC-RVOD products are therefore an optimal combination of RVOD and RO retrievals from the most comprehensive information in the CloudSat measurements. In our comparison we use IWC retrievals from RVOD products.

### 2.1.2 IWC from Aura MLS

The Aura MLS provides simultaneous measurements of $H_2O$, cloud IWC, temperature (T), and several trace gases [*Waters et al.*, 2006]. MLS observes microwave thermal emissions from atmospheric edge viewing forward along the orbital track, with a tangent point in front of the Aura satellite. The limb sounding has limitations in horizontal view, but is optimal for high-resolution vertical measurements. Aura MLS provides data profiles at 12 levels per decade change in pressure, i.e. 215, 178, 121, 100, 68 hPa, etc. We use MLS Version 2.2 (V2.2) Level 2 [*Livesey et. al.*, 2007] datasets in which IWC is retrieved from cloud-induced radiance ($T_{cir}$, the difference between measured radiance and modeled clear-sky radiance). A study by *Wu et al.* [2008]

validated the MLS IWC products. The validations of $H_2O$ and T are described by *Read et al.* [2007] and *Schwartz et al.* [2008].

MLS IWC must be screened using the status field in the collocated temperature profile to exclude bad retrievals [*Schwartz et al.*, 2008]. Besides temperature status and quality screening, a 2σ-3σ screening, where σ is the precision of single IWC measurement, derived on a daily basis, must also be applied in order to screen for noise (see the data quality and description document at http://mls.jpl.nasa.gov/data/v2-2_data_quality_document.pdf). Single IWC measurements from MLS have a vertical resolution of around 3 km and horizontal along-track and cross-track resolution of around 300 km and 7 km, respectively.

### 2.1.3 IWC from CALIPSO

The CALIOP onboard the CALIPSO is a polarization lidar at 532 nm and 1064 nm, provides retrievals of cloud and aerosol quantities such as extinction coefficients, optical depth, cloud and aerosol type, and cloud thermodynamic phase, etc. [*Winker et al.*, 2003]. CALIOP observes the atmosphere in nadir direction. Retrievals provide IWC in the Version 3 Release of Level 2 Cloud Profile (CPro) products at 60 m resolution vertically, 5 km resolution horizontally along-track, and resolution of the effective width of the laser beam across-track. IWC is derived applying the α-IWC-T relationship from *Heymsfield et al.* [2005] with visible extinction α calculated from the CALIPSO standard extinction algorithm [*Young and Vaughan*, 2009].

According to the Data Quality Statement issued on May 2010 (http://eosweb.larc.nasa.gov/PRODOCS/calipso/Quality_Summaries/CALIOP_L2Profile

Products_3.01.html), there are several substantial improvements in Version 3 cloud profile data products. Among the improvements, a newly developed five-dimensional PDF-based (probability density functions) Cloud-Aerosol Discrimination (CAD) algorithm classifies the feature types (e.g., cloud, aerosol, etc.) better than previous versions [*Liu et al.,* 2010]. This is important for our work because we only want to analyze scenes that are definitely classified as "clouds" but not "aerosols". The quality assurance parameter CAD Score provides a numerical confidence level for the classifications. A positive value of 100 indicates absolute confidence in the scene classification of cloud.

The other major improvement in Version 3 data is an entirely new developed algorithm for cloud thermodynamic phase discrimination [*Hu et al.*, 2009]. This algorithm classifies detected cloud layers as liquid water, randomly oriented ice (ROI), or horizontally oriented ice (HOI), based on relations between depolarization-backscatter thresholds and spatial coherence. The HOI and ROI are substitutes for mixed phase cloud and ice cloud respectively in previous Version 2 algorithm. Our study suggests a higher confidence on the retrieved IWC from ROI. This is because the non-depolarizing HOI particles yield anomalously large backscattering that makes extinction retrievals difficult, which makes the IWC derived from $\alpha$-IWC-T relationship unreliable. The feature types/subtypes and phase discrimination are stored in the atmospheric volume description (AVD) flag.

In our case, we only use IWC measurements from cloud that have a CAD Score of 100, and a cloud phase of ROI. Apart from AVD and CAD, quality assurance parameters such as the extinction quality control (QC) flags are also used to screen IWC.

For detailed data information and screen suggestions for using IWC, please refer to the CALIPSO cloud profile data quality statements.

2.1.4   Comparison

The retrieved IWC from these instruments may differ due to different viewing geometries and interrogated volumes and the use of different wavelengths. As indicated in Table 2.1, CloudSat R04 data correspond to a tangential volume over around $1.8 \times 1.4 \times 0.24$ km$^3$, and MLS V2.2 data correspond to a tangential volume over around 300 x 7 x 4 km$^3$, and the CALIPSO L2 data is of 5 km x 70 m horizontal spatial resolution at 60 m vertical resolution.

**Table 2.1.** Averaging volumes in different satellite data products.

|  | along-track (km) | across-track (km) | vertical (km) |
| --- | --- | --- | --- |
| MLS | 300 | 7 | 4 |
| CloudSat R04 | 1.8 | 1.4 | 0.24 |
| CALIPSO L2-05km | 5.0 | 0.07 | 0.06 |

To compare the data, we average data sets with finer spatial resolution to match the measurement volume of coarsest resolution, i.e., we average CloudSat and CALIPSO data to yield an equivalent measurement comparable to the MLS measurements.  Cross-track averaging is ignored in this case.  It should be noted that due to the A-Train satellite orbit path, CloudSat measurements are retrieved around 15 s ahead of CALIPSO and around 7 min ahead of Aura/MLS.  This is short enough that we will ignore the difference in time.

Inside the merging process, all CloudSat/CALIPSO IWC profiles within +/-150km (along-track) of a MLS tangent point are considered coincident with the MLS measurement. The coincident measurements are then averaged vertically within +/-1.5-km field-of-view of MLS height and then tangentially, to provide a single equivalent IWC for each MLS IWC measurement. The complete merging strategy is shown in Figure 2.2. Note that CALIPSO altitude (alt) and pressure (pres) are provided by GEOS-5 (Goddard Earth Observing System, version 5) meteorological products.

**Merging working flow…**

1. Reading process: read valid data from MLS (mls), CALIPSO (cal), and CloudSat (cs)…

| **mls Temp** | **CloudSat 2B-CWC-RVOD IWC** | **CALIPSO L2V3 IWC** |
|---|---|---|
| 1) geolocation<br>2) precision > 0<br>3) status = even<br>4) quality >0.6<br>5) convergence<=1.2 | 1) geolocation<br>2) RVOD_CWC_status<br>  bit2=0 (no precipitation)<br>  bit9=0 (small chi²)<br>  bit7=0 (good TAU input) | 1) geolocation<br>2) uncertainty <=2.0<br>3) extinct QC flag = 0 or 1<br>4) AVD bit1-3: type=2(cloud)<br>  bit6-7: phase=1(ROI) |

**mls IWC**
1) 2σ-3σ
2) geolocation
3) temp status = even

**valid mls data**
*H₂O, Temp, IWC coexist footprints (merging grid)*

**valid cs data**
*merged footprints*

**valid cal data**
*merged footprints*

**merging process**

2. Merging process: for each merging grid (on the same pressure (pres) level)…

**merging process**

**coincident cal footprints**
(±30min; along track 300km)

If true

For each coincident cal footprint

1. find closest *cal.pres* to *mls.pres*
2. get *cal.alt* on cal.pres level, take as *mls.alt*
3. *altLimit* = *mls.alt* ±1.5km
4. accumulate *altLimit*

**mean *altLimit***

For each coincident cal footprint → average *valid* IWC vertically within *altLimit* → v_iwc

average v_iwc along track → *cal.iwc*

**coincident cs footprints**
(±30min; along track 300km)

If true

For each coincident cs footprint → average *valid* IWC vertically within *altLimit* → v_iwc

average v_iwc along track → *cs.iwc*

**Figure 2.2.** The complete merging strategy of CloudSat (cs) and CALIPSO (cal) into MLS (mls). The first step is to read and screen data sets properly before going into merging process. The second step is to merge data sets using time, longitude, latitude, altitude, pressure etc.

Figure 2.3 shows a comparison of IWC at 121 hPa (~15 km) for the first week of
January 2009. The IWC shows consistent enhancements in the western Pacific, southern
Africa and South America.
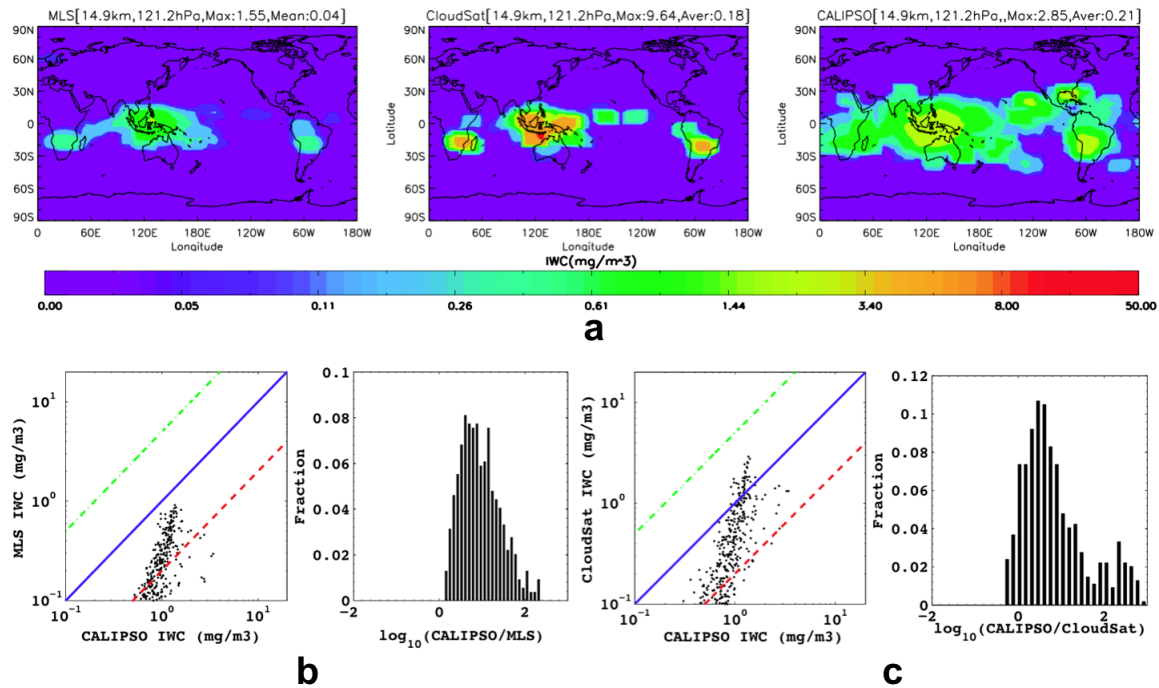


**Figure 2.3.** Merging IWC (>=0) comparison between MLS, CloudSat, and CALIPSO at approximately the
same volume for January 1-7, 2009. In upper panel **a**, the IWC are averaged on an $8^{o} \times 4^{o}$ Lon–
Lat grid, and a 3-point smoothing has been applied to the grid box averages. The lower left
panel **b** is a scatter plot of CALIPSO vs. MLS, ratio distribution of CALIPSO/MLS; lower
right panel **c** is a scatter plot of CALIPSO vs. CloudSat, and the ratio distribution of
CALIPSO/CloudSat. The blue solid line shows 1:1 ratios; the red and green dash lines show
5:1 and 1:5 ratios, respectively.

On average, MLS detects the lowest IWC. CloudSat mean IWC is 3-4 times
greater than that of MLS, due to MLS sensitivity degradation at large ice particles [*Wu et
al.*, 2009]. Meanwhile, CALIPSO measurements are larger than that of MLS in most of
the area. Part of the reason is that MLS has difficulty to penetrate through all clouds

along the path due to further attenuation away from the instrument.  Also, CALIPSO can see small particles that MLS misses.

CloudSat has the smallest area with detectable IWC, whereas CALIPSO covers the largest.   The reason is that at higher altitude like ~15 km, most of the clouds are cirrus clouds with small amount of IWC (see Section 4).  The CloudSat is insensitive to these particles but they are easily detectible by CALIPSO.  This can also be observed in the lower panels with scatter and ratio plots of nonzero IWC measurements from MLS, CloudSat, and CALIPSO.  From the plots of CALIPSO versus MLS (panel b), it is shown that CALIPSO IWC are greater than that of MLS for most of the cases.  Lower right panel c shows CALIPSO versus CloudSat.   There are large areas where CALIPSO detects ice but CloudSat does not; the IWC are larger for CALIPSO in these areas.

The above results should not come as any surprise. Compared with MLS and CALIPSO, CloudSat has better cloud penetrating ability with the radar, so it can detect and measure optically thick ice clouds without being strongly attenuated [*Wu et al.*, 2008, 2009; *Schwartz and Mace*, 2010].  But it is not the case when detecting cirrus.  Studies by *Comstock et al*. [2002] and *Sassen et al*. [2009] concluded that the optically thin and cold cirrus could go entirely undetected by radar, especially those tropical cirrus clouds that are thin optically or laminar in appearance.  As previously discussed, operationally, it is well established that lidar is better suited than even the most sensitive millimeter-wave cloud radar for detecting cold, optically thin cirrus clouds [*Comstock et al.*, 2002; *Sassen*, 2002].  Our results support the common arguments.

The difference in ice cloud detection between radar and lidar is mainly due to the fact that the wavelength of the incident electromagnetic wave in radar is larger than the

size of most cirrus cloud particles. This makes the particles behave as Rayleigh scatterers with radar backscattering dominated by the particle diameter-to-the-sixth power law. On the contrary, lidar backscattering is proportional to the diameter squared because the wavelength is smaller than the particles. Small particles whose diameters differ by a factor of 2 may result in radar cross sections differ by a factor of 64, and in terms of radar echo power, the difference will be ~18dB [*Sassen et al.*, 2009]. Therefore, when observing the same clouds, lidar views higher cloud tops than the radar does because of its great sensitivity to small hydrometeors; meanwhile, radar can penetrate deeper into clouds with little or no attenuation.

The above comparison results further prove that CALIPSO lidar observation of cirrus clouds is most suitable for our study since most of the TTL cirrus clouds that we focus on are substantially thin and high. For most of the parts in our study, we will use IWC from CALIPSO Level 2 V3 Cloud Profile (CPro).


## 2.2 Other datasets besides IWC

The other key factor in our analysis is the estimate of maximum $H_2O$ abundance available for in situ cirrus formation. We will infer this vapor abundance from both CALIPSO and MLS measurements in different standpoints.

When deriving $H_2O$ from CALIPSO datasets, optical depth($\tau$) measured by CALIOP, GEOS-5 reanalysis temperature (T) and pressure (P) information are also used (see next section). The optical depths are obtained by integrating the 532 nm cloud extinction profile. We performed the similar screen of optical depth data by inspecting the extinction quality control (QC) flags, CAD Scores, and cloud phase. The estimated

uncertainty in the column optical depth can be found in CALIPSO Version 3 Extinction Uncertainty Document[1]. Temperature and pressure are derived from GEOS-5 reanalysis data products provided by Global Modeling and Assimilation Office (GMAO) Data Assimilation System. The GEOS-5 reanalysis products provide updated atmospheric state information four times daily at 00Z, 06Z, 12Z, and 18Z, using optimal combinations of model forecasts and observations. Detailed data uses and validations can be found in the GEOS-5 documentation[2] by *Rienecker et al.* [2008].

MLS $H_2O$ is retrieved from calibrated radiance observations by the MLS data processing algorithms [*Livesey et al.*, 2006; *Jarnot et al.*, 2006] and validated by *Read et al.* [2007]. It is produced at the same pressure surfaces as other MLS fields. MLS $H_2O$ has 10% accuracy, which means that if MLS data gives 5 ppm in concentration of $H_2O$, 4.5-5.5 ppm will be the range that can be considered possible. Further details please refer the following section.

## 2.3    Summary

To summarize, for our topic of study, we will analyze CALIPSO v3.1 Level 2 (http://www-calipso.larc.nasa.gov/) Cloud Profile (CPro) datasets as well as MLS v2.2 Level 2 [*Livesey et al., 2007*] water vapor mixing ratio ($H_2O$), ice water content (IWC), and temperature (T) datasets. Our analysis will cover the period from December 2008 through November 2009 for a complete seasonal cycle. GEOS-5 data interpolated into CALIPSO data grids will provide meteorological parameters.

---

[1]http://eosweb.larc.nasa.gov/PRODOCS/calipso/pdf/CALIOP_Version3_Extinction_Error_Analysis.pdf
[2] http://gmao.gsfc.nasa.gov/pubs/docs/GEOS5_104606-Vol27.pdf

# 3.    METHODOLOGY

From Section 1 we understand that cirrus clouds in the TTL could form either in situ or as blow-off from convective anvils.  The key point for distinguishing the convective cirrus is to find how much $H_2O$ is available in the ambient air for in situ cirrus formation.  This brings up another question: $H_2O$ within the TTL is not strictly even distributed anywhere; it might have different vapor amount in different area.  For example, in the TTL, $H_2O$ above the cold tropical western Pacific is usually lower than the other regions.

To make it general, we find the maximum amount of $H_2O$ available in the ambient air through the whole tropics.  Under extreme conditions that if all $H_2O$ condenses into ice, this will give us an upper limit of IWC as our threshold.  In this way, cirrus clouds that have IWC beyond this threshold must come from deep convection.  For example, the maximum amount of $H_2O$ available around the tropopause is about 5 parts per million by volume (ppmv), then measurement of cirrus IWC indicating 20 ppmv definitely comes from convective anvil blow-off.  However, for clouds that contain less IWC than is available in the ambient gas phase, they cannot be uniquely assigned with a formation mechanism—they may either form in situ or still be of convective origin but have thinned out.

Noted that because the IWC thresholds come from two steps of maximization (maximum amount of $H_2O$ through the entire tropics and maximum condensation of all available $H_2O$ into ice), they are upper limits and they generate lower fractions of

convective cirrus. Therefore, all fractions in this study could be higher, but the values we provided are the ones that we are most confident of.

We emphasize that in our analysis, we use the volume mixing ratio (VMR) to express the abundance of a constituent. Conceptually, the VMR of a constituent is the fraction of molecules in a given volume that are this constituent. The VMR is the ratio of the number density of a constituent to the total number density. While the number density of a constituent changes when temperature or pressure in an air mass change, the VMR does not. In other words, the VMR is conserved for changes in the pressure or temperature of a parcel, which makes VMR very useful. Because the VMR is typically small, it is usually multiplied by $10^6$ or $10^9$ to obtain parts per million by volume (ppmv) or parts per billion by volume (ppbv). For example, a VMR of $5 \times 10^{-6}$ or 5 ppmv of $H_2O$ means that 5 out of every $10^6$ molecules in a sample are $H_2O$ molecules. Unless noted otherwise, we will always use VMR but not added v. It should be clear that the unit ppm in our analysis indicates parts per million by volume.

We use two methods to infer the maximum amount of $H_2O$ available for in situ cirrus formation. This is the most critical calculation in our analysis and this value represents our threshold. Two methods based on measurements from different satellites yield two sets of thresholds. They are consistent and verifiable, as will be shown below.

## 3.1    Vertical coordinate

Before explaining our methods, we emphasize that potential temperature is chosen as our vertical coordinates because in the TTL, saturated water vapor mixing ratios are typically very low due to extremely low temperatures. At low water mixing

ratios, heat release from water phase change is small compared to radiative heating. Therefore, air parcels can effectively be treated as dry. Thermodynamic processes in this layer are approximately adiabatic [*Danielsen et al.*, 1993] and horizontal flow roughly follows an isentropic surface.
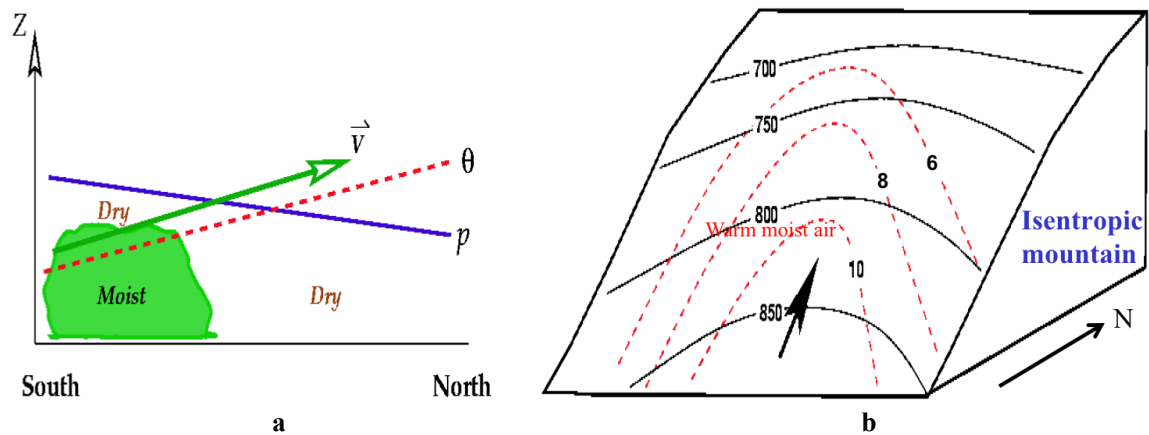


**Figure 3.1.** Schematic illustration of isentropic surfaces and moisture advection along them. Panel a: moist air from low levels on the left is transported upward and to the right along the isentropic surface. (Adapted from Bluestein, vol. I, 1992, p.23). Panel b: moist air flows along the isentropic surface from south to north, with humidity decreases. The solid black lines are isobars in hPa, and the dashed red lines are isohumes (constant mixing ratio) in g/kg. Adapted from Millersville University Isentropic Workshop by James T. Moore, 2003.

As shown in Figure 3.1, the advantage of representing meteorological conditions on isentropic surfaces is that horizontal flow along an isentropic surface already contains the adiabatic component of vertical motion (panel a). Besides, the moisture transport occurs along isentropic surfaces (panel b).

Our work mainly focuses on four isentropic levels: i) 357 K, the bottom of TTL, which is close to the typical level of neutral buoyancy (LNB) of deep, tropical convection [*Folkins et al., 1999*]; ii) 365K, halfway between TTL bottom and the tropopause; iii)

375 K, near the cold-point tropical tropopause; and iv) 390 K, which our study suggests is approximately the highest level that has statistically detectable cirrus clouds in CALIPSO data.

## 3.2    MLS H$_2$O method

Our first method is based on the MLS direct measurements of water vapor concentration ([H$_2$O]) in the TTL air.  MLS data profiles are provided at 12 levels per decade change in pressure from ground to 21.5 hPa.  Therefore, in this method we find the threshold at different isobaric surfaces.

Figure 3.2 depicts a global five-year mean temperature and water vapor abundance at 100 hPa.  The 100 hPa surface in the tropics is close to the tropical tropopause (about 375 K in potential temperature or 17 km in altitude).  Unlike in the lower atmosphere, H$_2$O is nearly uniformly distributed in the tropical tropopause. Concentrations of H$_2$O around the tropics are usually between 3.7 ppm and 4.4 ppm, with an exception over the western Pacific region, where concentration of H$_2$O is less than 3.4 ppm due to lower temperature there.  This supports the theory that T controls humidity near the tropical tropopause [*Holton and Gettelman*, 2001].
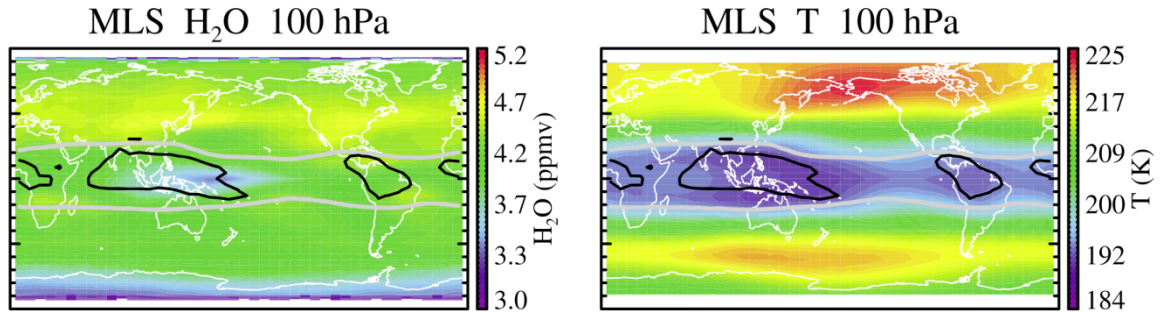
**Figure 3.2.** A five-year mean (January 2005 to December 2009) annual $H_2O$ and T maps at 100 hPa from MLS datasets. Black contours enclose GEOS-5 OLR of 240 Wm$^{-2}$ or less (regions of deep convection). Adapted from *Jiang et al.* [2010].

We define MLS measurements of non-zero IWC as cloudy and zero IWC as cloud-free. The $H_2O$ abundance in cloud-free air is then considered as $H_2O$ available in ambient air to form in situ cirrus. The first two plots in Figure 3.3 show the probability density functions (PDFs) and cumulative density functions (CDFs) of cloud-free air temperature (T) and [$H_2O$] measurements at 100 hPa (close to the tropopause) during boreal winter (DJF). We see that ambient air usually has T ranging from 187 to 200 K with mean 193 K, and most probably with T of 192 K (first panel). The second panel shows that the retrieved [$H_2O$] is generally between 1.6 ppm and 5.4 ppm with mean 3.3 ppm, and most probably at 3.0-3.4 ppm, but never exceeds 6 ppm.
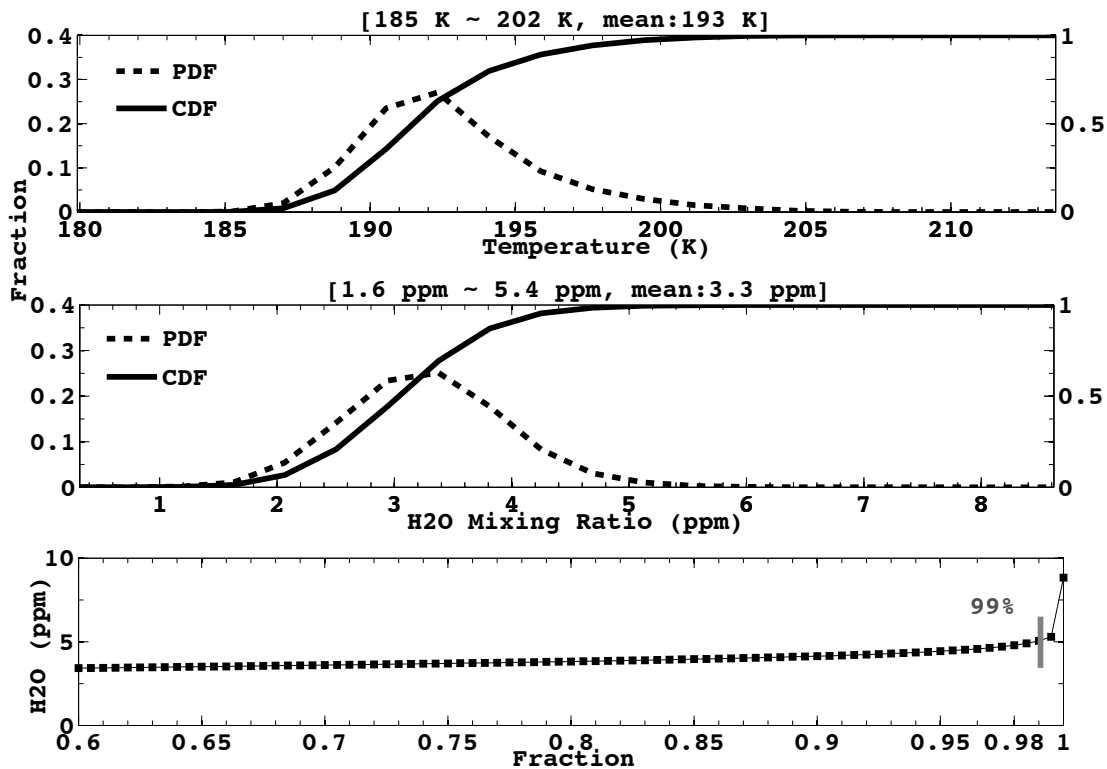
**Figure 3.3.** MLS cloud-free observations at 100 hPa (close to the tropical tropopause) during boreal winter. The upper two panels are PDFs and CDFs of temperature and $H_2O$ mixing ratio ($[H_2O]$). Dashed lines show PDFs in left-y axis and solid lines show CDF in right-y axis. The third panel shows the magnified cumulative $[H_2O]$ fraction from 0.6 to 1.0. Finally, we choose 99% of clear air measurements that have $[H_2O]$ below 5.1 ppm as our MLS $H_2O$ threshold.

The third panel is a magnification of cumulatively over 60% of $[H_2O]$. We see that before reaching above 99%, $[H_2O]$ is very steady and less than 5.1 ppm. Therefore, we choose 99% of clear air observations with $[H_2O]$ below 5.1 ppm as our MLS $H_2O$ threshold. This is the expected maximum IWC that can be found within cirrus formed through in situ adiabatic cooling. Beyond this threshold, cirrus clouds must have originated from convective anvil blow-off, and are therefore categorized as convective cirrus in our analysis.

### 3.3 CALIPSO T-Dependent method

Our second method is based on CALIPSO datasets. Different from MLS, CALIPSO does not measure $H_2O$ directly. But we know the truth that temperature controls humidity (see Figure 3.2), thus, find the maximum amount of $H_2O$ in ambient air for in situ cirrus formation is equivalent to find the highest temperature that in situ cirrus could have. This is the critical temperature ($T_c$) that below $T_c$, we see abundant cirrus formed in situ, whereas above $T_c$ we barely see any in situ cirrus. Therefore, we name this method as the CALIPSO T-Dependent method.

In this method, the thresholds are derived from using CALIPSO observations of cirrus IWC and optical depth, and meteorological parameters are provided by GEOS-5 reanalysis datasets. The cirrus are referred as the measurements that show "cloud" (not "aerosol") from the CALIPSO Cloud-Aerosol Discrimination (CAD) algorithm, and show "cirrus" from the definition by the International Satellite Cloud Climatology Project (ISCCP) at the same time (refer the CALIPSO data statement). We take these cirrus clouds as our data basis to perform identification. It turns out that CALIPSO is very efficient in detecting cirrus. The detailed cirrus observations from CALIPSO can be found in the next section.

Since this method is based on temperature, it is necessary to understand the characteristics of temperature in the TTL. A global view of seasonal temperature variations at 4 isentropic surfaces is depicted in Figure 3.4. The plots show that low temperatures are always located in the deep tropics, particularly the tropical western Pacific, where both in situ and convective cirrus exist [e.g., *Comstock et al.*, 2002; *Winker and Trepte*, 1998]. In the tropics, the coldest season is DJF and the warmest

season is JJA. Temperatures tend to increase above 375 K in all seasons as well as the
entire year, which indicates that 375 K potential temperature is close to the cold-point
tropopause, where the temperature minimum is found.
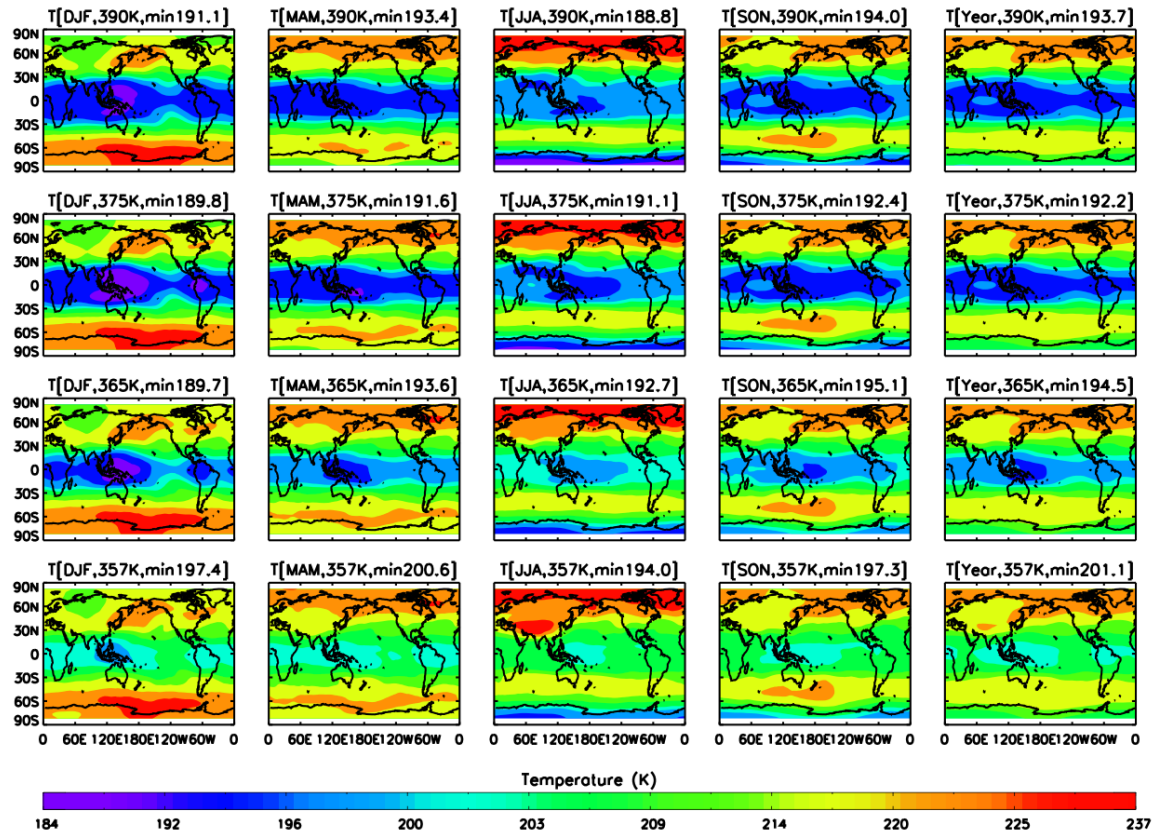


**Figure 3.4.** Seasonal temperature variations in isentropes from GEOS-5 reanalysis data (provided in CALIPSO datasets). The five columns, from left to right, are December-January-February (DJF), March-April-May (MAM), June-July-August (JJA), September-October-November (SON), and annual (year) respectively. From lower to upper the four isentropic levels are 357 K, 365K, 375K, and 390 K, respectively.

For finding the in situ cirrus, we pick optically thin cirrus measurements, so as to exclude convective clouds.  Here we use the definition of "thin" as optical depth $\tau<=0.3$ (*Sassen and Cho*, 1992). Then the associated $T_c$ is the upper limit of temperature in which these in situ cirrus clouds can still be found.  Above $T_c$, we barely see in situ cirrus.

Figure 3.5 shows the PDFs and CDFs of altitude, pressure, and temperature of optically thin cirrus at 375 K, approximately the level of tropical tropopause, during boreal winter.  Results suggest that at the tropopause, most thin cirrus occur at least 16.7 km above mean sea level and at most 17.4 km, and most probably at 17.1 km.  At this high altitude, pressure is usually lower than 100 hPa, mainly between 91 and 98 hPa. Thin cirrus are then extremely cold, usually around 191 K, with the lower limit at 188 K and the upper limit at 194 K, indicating that most thin cirrus form at least below 194 K and most likely at 191 K.  We may choose the warmest temperature of 194 K as our critical temperature ($T_c$).

**CALIPSO Thin Cirrus Cloud at θ=375K [DJF, Tropics]**
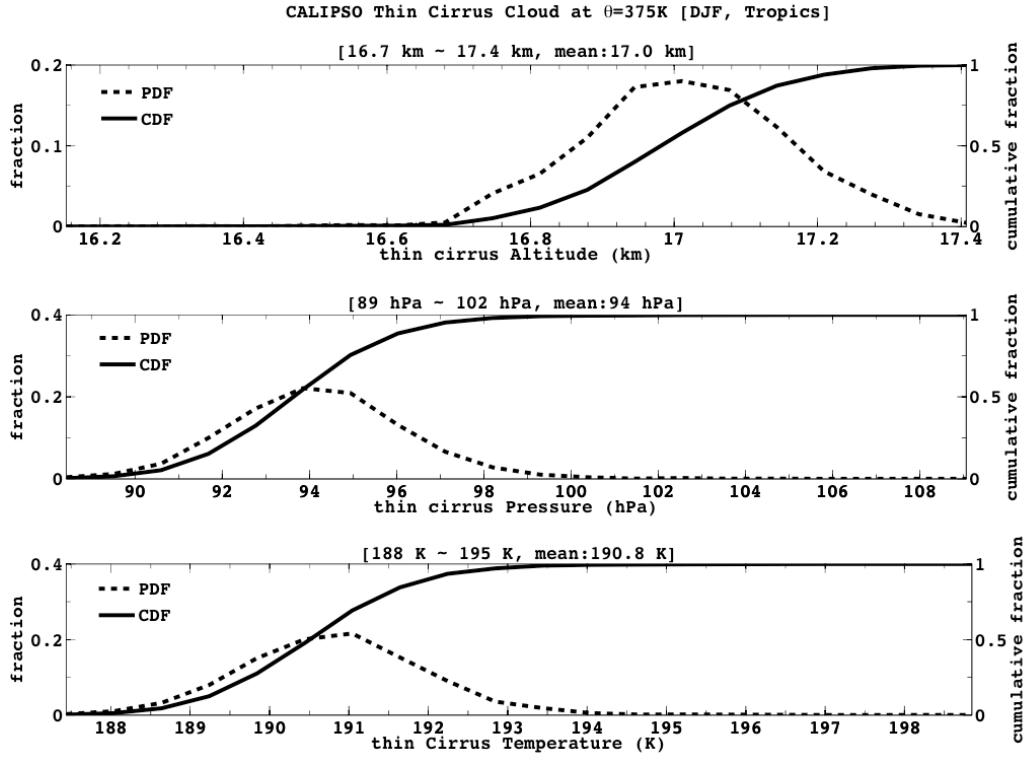


**Figure 3.5.** PDFs and CDFs of altitude, pressure, and temperature of CALIPSO thin cirrus at 375 K level during boreal winter. Dashed lines show PDFs in left-y axis and solid lines show CDFs in right-y axis.

Given this critical temperature $T_c$, we can infer the theoretically maximum amount of $H_2O$ at which the air reaches to saturation, i.e., the saturation mixing ratio at $T_c$ ($[H_2O(T_c)]_s$ ). $[H_2O(T_c)]_s$ is then referred as our T-Dependent threshold, which is the maximum IWC could exist within in situ cirrus if ambient $H_2O$ completely condensed through in situ adiabatic cooling.

It should be noted that we calculate the saturation vapor pressure with respect to ice ($e_{si}$) using the relation from *Murphy and Koop* [2005] (see appendix), as shown below

$$e_{si}\,(T_c) = exp(9.550426 - 5723.265/\,T_c + 3.53068\,ln(T_c) - 0.00728332\,T_c) \quad \text{(i)}$$

where $T_c$ in units of Kelvin and $e_{si}$ in units of Pa. As the equation indicates, saturation vapor pressure is only dependent on temperature. As we mentioned earlier, we use volume saturation mixing ratio in our analysis, then $[H_2O(T_c)]_s$ is the ratio of $e_{si}$ over the actual pressure (P) of the air. To make it clear, we multiply it by $10^6$ to obtain parts per million (ppm).

Figure 3.6 illustrates the $[H_2O(T_c)]_s$ dependence with temperature from Figure 3.5. Results further reveal that $[H_2O(T_c)]_s$ increases monotonically with increasing temperature. For example, 80% of thin cirrus clouds have temperatures less than 191.7 K, if take this value as critical temperature, when reaching to saturation, the maximum amount of water vapor ($[H_2O(T_c)]_s$) will be 4.5 ppm; 90% of thin cirrus clouds have temperatures less than 192.3 K, in which the associated $[H_2O(T_c)]_s$ is 4.9 ppm. For the top 2%, temperature jumps abruptly and reaches to almost 200 K, and the associated $[H_2O(T_c)]_s$ increases to a maximum of 13 ppm. The most likely reason for this long tail may be that there is error in the GEOS-5 reanalysis data. To avoid the exceptions, we eliminate the top 2% but still pick up the relatively conservative 98% threshold, which yields 193.4 K as $T_c$ and the associated $[H_2O(T_c)]_s$ of 5.8 ppm to be our threshold value. Compared to this threshold, higher IWC in cirrus clouds are not likely to come from in situ, and therefore must come from convection.
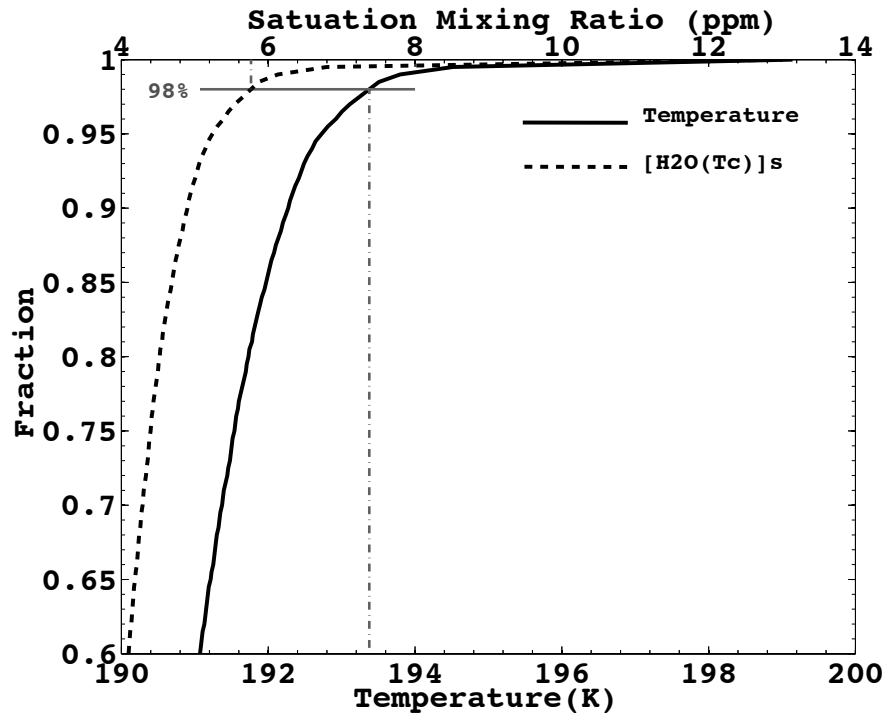
**Figure 3.6.** Thin cirrus temperature (solid line) and the associated H2O saturation mixing ratio (dashed line). 98% of thin cirrus has a temperature below 193.4 K, then a vapor saturation mixing ratio of 5.8 ppm is chosen as our threshold.

## 3.4    Thresholds comparison

Table 3.1 summarizes the thresholds derived from both methods. Note that MLS thresholds are obtained at isobaric surfaces, whereas the T-Dependent thresholds are derived at isentropic levels. To compare them, we choose the levels with closest temperature range because temperature is the key factor controlling $H_2O$ abundances in the TTL. Temperature from both datasets are validated in *Jiang et al.* [2010] and they concluded that both temperatures agree on average to within ~0.5 K above 147 hPa (close to the TTL bottom), which guarantees the accuracy of our work. These thresholds indicate, from different perspectives, the maximum possible IWC that can be found within cirrus formed in situ.

**Table 3.1.** Thresholds comparison (DJF, tropics) at nearly the same levels.

| CALIPSO $\theta$ (T) / $[H_2O(T_c)]_s$ | MLS P (T) / $[H_2O]$ |
|---|---|
| **390 K** (190-197 K) / 7.7 ppm | **83 hPa** (181-201 K) / 5.0 ppm |
| **375 K** (188-195 K) / 5.8 ppm | **100 hPa** (187-200 K) / 5.1 ppm |
| **365 K** (187-203 K) / 11.9 ppm | **121 hPa** (191-206 K) / 9.1 ppm |
| **357 K** (195-206 K) / 22.2 ppm | **147 hPa** (198-209 K) / 19.6 ppm |

Generally, CALIPSO T-Dependent method yields higher thresholds. This could be caused by errors in GEOS-5 reanalysis data because this method is highly dependent on reanalysis data. Error of 1 degree could make huge difference. Or, it could be the MLS $H_2O$ that is around 10% in accuracy. Besides, we have to realize the fact that they are not at exactly the same surfaces.

MLS threshold at 100 hPa is similar to that of the CALIPSO threshold at 375 K. This should not come as a surprise because 375 K and 100 hPa are both near the tropical tropopause. Below the tropopause both thresholds show versa similar trend (thresholds at lower levels tend to be higher and at upper levels tend to be lower). This trend is especially prominent at lower isentropic levels (357-365 K) where warmer air leads to higher $[H_2O]$ because temperature dominates the air's ability to hold vapor. Above the tropopause, the critical temperature increases, resulting in higher values of $[H_2O(T_c)]_s$. This is not featured in MLS data, which may partly be due to the large averaging volumes of MLS data.

# 4.    IDENTIFICATION RESULTS

In Section 3, we developed two methods to infer theoretical maximum amounts of water vapor ($H_2O$) available in ambient air for in situ cirrus formation, which serve as our thresholds. We concluded that cirrus with an IWC higher than the threshold must be of convective origin. Now, we ask the following questions: What fraction of TTL cirrus originates from convection if we apply the thresholds? What is their distribution pattern? What is the seasonal variation of their distribution? The following will serve to answer these questions.

## 4.1    Cirrus distributions revealed in CALIPSO data

Before analyzing the identification results, it is necessary for us to have a general picture of TTL cirrus observed by CALIOP. Many studies have studied the distribution of tropical cirrus using CALIPSO datasets because CALIOP is capable of detecting optically thin and high clouds. The study by *Sassen et al*. [2008, 2009] identified cirrus with optical depths no greater than 3.0 and cloud top temperatures less than -40$^o$C. *Nazaryan et al*. [2008] used the Cloud Layer (CLay) data products to identify cirrus based on Feature Classification Flags indicating cloud and layer base height higher than 8 km. A study by *Schwartz and Mace* [2010] took layer base above 14 km and geometrical thickness no greater than 3 km to focus on TTL cirrus. Similarly, *Riihimaki and McFarlane* [2010] identify TTL cirrus based on the criteria that cloud base heights are greater than 14 km and optical depths are less than 0.4. Although many techniques are

employed to identify cirrus, the results of these techniques are generally similar and consistent.

In our study, we identify cirrus clouds using the CALIPSO Cloud Profile (CPro) datasets of both daytime and nighttime measurements. Recall that CPro datasets provides feature type of "cloud" and subtype of "cirrus" or "deep convective cloud" classifications. According to the quality statements of Version 3 CPro data, cloud subtypes are defined by the International Satellite Cloud Climatology Project (ISCCP) based on the combined measurements of cloud top altitude, cloud ice/water phase, cloud opacity, and cloud fraction within an 80 km segment.
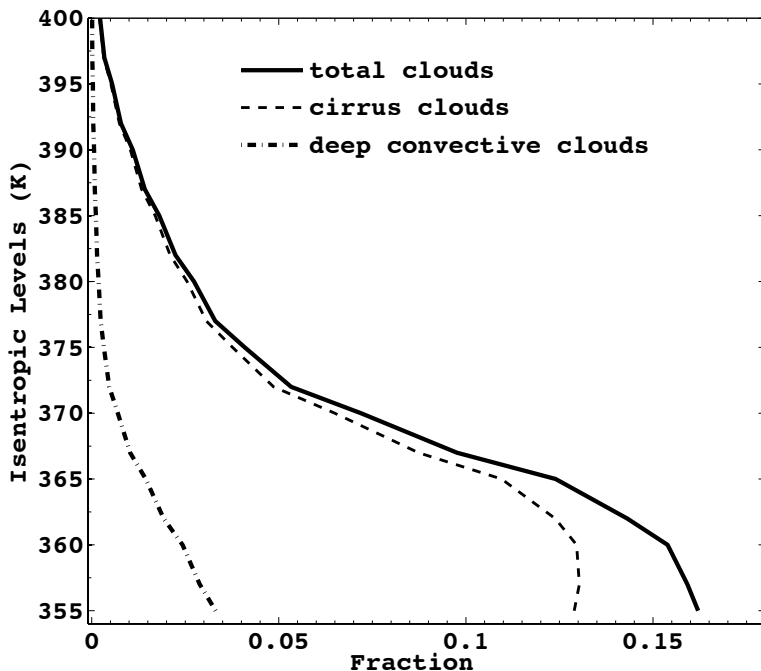


**Figure 4.1.** Annual fractions of tropical (30°S-30°N) total clouds, cirrus clouds, and deep convective clouds revealed in the CALIPSO CPro datasets. Cloud fractions are the ratio of number of measurements classified as cloud over total number of measurements; cirrus fractions are obtained the same way except here we count the number of measurements flagged as cirrus. So as convection fractions.

Figure 4.1 shows the annual fractions of total clouds, cirrus clouds, and deep convective clouds in the tropics ($30^{o}$S-$30^{o}$N) from 355 K to 400 K in bins of 2.5 K, as measured by CALIOP.  At each isentropic level, the total cloud fraction is the ratio of the number of measurements indicating cloud over the total number of measurements at that level throughout the entire year (December 2008 to November 2009).  Cirrus cloud fraction is obtained in a similar way, except by counting the number of clouds flagged as cirrus at that level.  Results show that the cloud fractions of all clouds and cirrus clouds decrease with increasing height.  Maximum cirrus fractions occur between 357 K and 362 K (around the TTL bottom), which is between 14.7 and 16.2 km, agreeing with other works such as *Eguchi et al.* [2007], *Nazaryan et al.* [2008], and *Riihimaki et al.* [2010]. Through the entire TTL, cirrus frequency is close to cloud frequency, especially above 375 K where almost all clouds are categorized as of cirrus type, which agrees well with common knowledge.  Of the remaining clouds, most are deep convective clouds (dash-dotted line).  This result indicates that most of the clouds in the TTL are either cirrus or deep convective clouds, which agrees with our discussion of cirrus formation in Section 1.
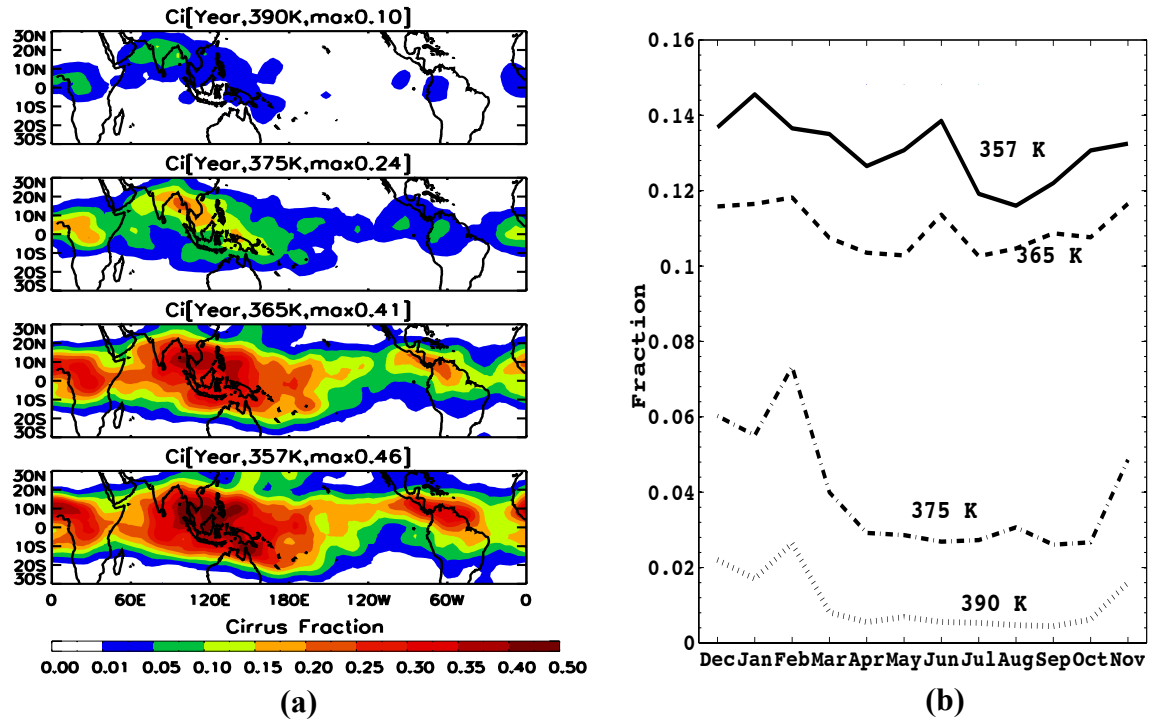
**Figure 4.2.** Fractions of occurrence of TTL cirrus at four isentropic levels viewed from CALIOP. (a) Annual fraction maps are plotted with fractions obtained on 4°x2° Lon-Lat grid boxes and a 3-point smoothing from December 2008 to November 2009. (b) Monthly fractions at tropical regions (30°S-30°N).

Figure 4.2 shows the fraction of occurring cirrus at four isentropic levels within the TTL, as viewed from CALIOP. The annual fraction maps are plotted with fractions obtained from 4°x2° Lon-Lat grid boxes and 3-point smoothing. To be noted that the following fraction maps are all obtained in the same manner. From panel a, we see that the highest fraction of occurrence of cirrus is collocated over the equatorial Africa, tropical western Pacific, and northern South America throughout the TTL. This result is consistent with many previous works, such as *Massie et al.* [2002], *Dessler et al.* [2006], and *Sassen et al.* [2008, 2009]. Cirrus clouds occur more often in the lower TTL than in the upper TTL, especially when the tropopause (375 K) is encountered where frequency of occurrence drops down abruptly. This result agrees with previous studies such as

*Wang et al.* [1996], *Fu et al.* [2007], and *Massie et al.* [2010]. The highest frequency of cirrus is found over the tropical western Pacific near the bottom of the TTL (357 K). The annual averages of fractions, represented by the total number of cirrus measurements over total number of measurements, at 357 K, 365 K, 375 K, and 390 K are 0.20, 0.18, 0.11, and 0.07, respectively.

The monthly tropical (30°S-30°N) cirrus frequencies at different isentropic levels show a similar trend, as the highest fractions occur during boreal winter and the lowest occur during boreal summer. At and above the tropopause, starting in March, the occurrence of TTL cirrus becomes less frequent until the end of October. At lower TTL, occurrence of cirrus in May and July is heavily influenced by the Indian and Southeast Asian monsoon, which makes the frequency higher than adjacent months.

Figure 4.3 shows the seasonal vertical fractions of cirrus clouds (panel b). In order to best interpret the seasonal variations we also include total clouds fractions (panel a) as well as temperature profiles (panel d). Cirrus clouds, as well as total clouds, occur in the TTL following the same trend, in that they are most frequent during the boreal winter (brown line) and least frequent during the boreal summer (red line). This agrees well with many previous studies such as *Mergenthaler et al.* [1999] and *Massie et al.* [2003, 2010]. The less frequent occurrence of cirrus in JJA can be attributed to both warmer temperatures near the tropical tropopause and less frequent deep convections, and vice versa [*Reed and Vlcek*, 1969]. From our previous discussions we know that most of the clouds in the TTL are cirrus clouds. This is further verified in panel c, where fraction profiles of cirrus (dashed lines) and total clouds (solid lines) are similar throughout all seasons at nearly all isentropes, especially above the tropical tropopause (375K). The

seasonal variations in the temperature profiles shown in panel d present a trend opposite

of that of the cirrus occurrence: the lowest temperatures in DJF correspond to the highest

frequency of occurrence of cirrus, whereas highest temperatures in JJA correspond to the

lowest cirrus frequency.
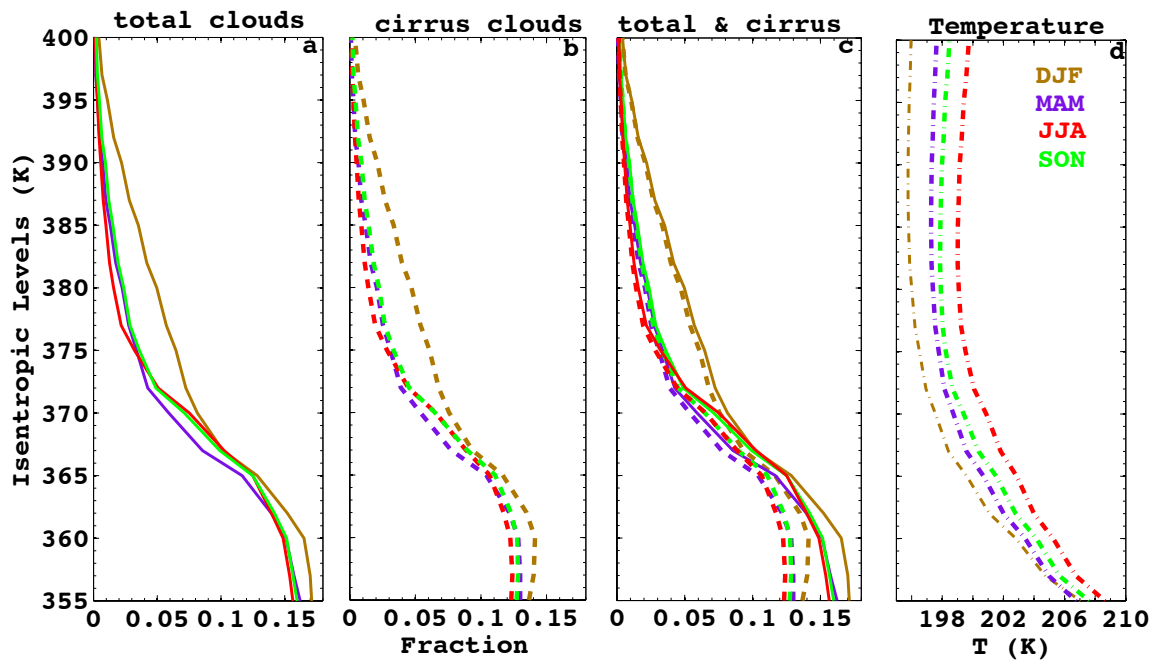


**Figure 4.3.** Seasonal fraction variations of total and cirrus clouds recorded in CALIPSO CPro datasets. Yellow, purple, red, and blue represent season DJF, MAM, JJA, and SON, respectively.

Overall, many distinct features of TTL cirrus can be found in CALIPSO observations. They agree well with other datasets, which gives us confidence in using the datasets provided for further analysis. Then, we are ready to identify those cirrus clouds of convective origin.

## 4.2    Convective cirrus distributions revealed by CALIPSO

4.2.1    Overview of convective cirrus in boreal winter (DJF)

Cirrus clouds with IWCs higher than thresholds are categorized as of convective origin. Here when we comparing IWC with thresholds, we converted CALIPSO cirrus IWC from $g/m^3$ to volume mixing ratio (ppm) using the temperature and pressure provided from reanalysis data (see Appendix for details of converting). Figure 4.4 shows the fraction maps of occurrence of TTL cirrus (first column) and convective cirrus in boreal winter (DJF) at four isentropic levels, in which we apply both the T-Dependent thresholds (second column) and MLS $H_2O$ thresholds (third column). Within each grid box, convective cirrus fraction is defined as the number of cirrus measurements identified as of convective origin over the total number of cirrus measurements. The fraction maps are obtained in the same manner as in Figure 4.2 a.
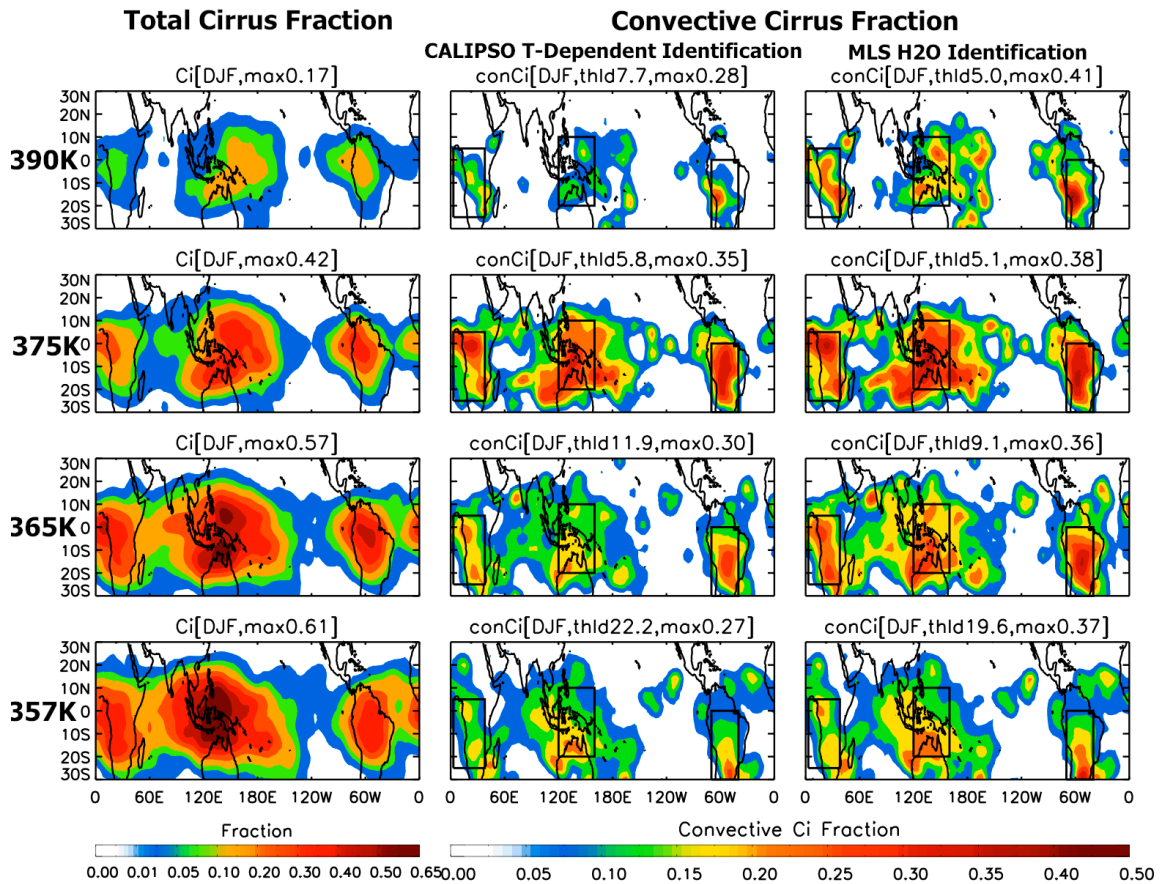
**Figure 4.4.** Cirrus and convective cirrus fraction maps from 2008 December to 2009 February. Fractions are averaged on $4^o$x$2^o$ Lon-Lat grid boxes and 3-point smoothing has been applied to the grid box averages. Three rectangles mark are three most enhanced convective cirrus regions: equatorial Africa, tropical western Pacific, and northern South America.

At all isentropic surfaces, we observed highest fraction of boreal winter cirrus occur in the same regions as in annual maps (Figure 4.2), but with enhanced values. This supports our previous conclusion that cirrus occurrence during boreal winter contributed much to the annual average, i.e., cirrus clouds occur more often during DJF (Figure 4.3). Especially at the TTL bottom (~357 K), we observed a frequency maxima appear at the tropical western Pacific, reaching to 61% within a $4^o$x$2^o$ Lon-Lat grid box. This agrees well with results reported in *Sassen et al.* [2008].

Throughout the TTL, both methods of identifying convective cirrus show the same overall patterns as well as good quantitative agreement. In Figure 4.4, we also found that continental regions have the most frequent occurrence of convective cirrus clouds, which is consistent with the knowledge that deep convection occurs more frequently over land. The fraction of occurrence of convective cirrus can be observed up to 0.27, 0.30, 0.35 and 0.28 by applying the T-Dependent thresholds, respectively, from 357 K to 390 K.

Three most enhanced regions of convective cirrus are marked with rectangles on fraction maps. They mainly reside in the regions with the most frequent total cirrus. The frequency variations of convective cirrus by T-Dependent thresholds within three rectangles are illustrated in Table 4.1. For comparison, we also averaged around the tropic region ($30^{o}$S-$10^{o}$N).

**Table 4.1.** Regional frequency differences of convective cirrus by applying CALIPSO T-Dependent thresholds at different isentropic levels (DJF).

| | Africa region $3^{o}$E~$38^{o}$E, $25^{o}$S-$5^{o}$N | western Pacific region $120^{o}$E-$160^{o}$E, $20^{o}$S-$10^{o}$N | South America region $70^{o}$W-$40^{o}$W, $30^{o}$S-$10^{o}$N | tropic region $30^{o}$S-$10^{o}$N |
|---|---|---|---|---|
| 390 K | 12.1 % | 10.3% | 7.9% | 8.5% |
| 375 K | 23.2% | 25.5% | 24.1% | 20.1% |
| 365 K | 16.4% | 15.5% | 17.6% | 13.1% |
| 357 K | 12.5% | 14.3% | 11.9% | 11.2% |

From Table 4.1, at each level there is little regional difference as to the frequency maxima. It can be found in western Pacific region at 357 K (14.3%) and 375 K (25.5%), or South America region at 365 K (17.6%), or it can also be found in Africa region at 390 K (12.6 %). Note that the frequencies we obtained may depend on the area where boxes

enclosed. But frequencies in each region all show a maximum at 375 K level, which builds our notion that convective cirrus occur most frequently near the tropical tropopause. This is further supported by the higher fraction averaged around the entire tropics. Overall, from high to low the fractions show a vertical trend from 375 K, 365 K, 357 K, to 390 K.

For convective cirrus identified by the MLS $H_2O$ thresholds, the fraction maxima appear in the same regions but show higher values, due to the fact that MLS $H_2O$ thresholds are generally lower. For example, T-Dependent thresholds yield average frequencies in tropic area from $30^oS$ to $10^oN$ of 11.2% (357 K), 13.1% (365 K), 20.1% (375 K), and 8.5% (390 K), respectively. By applying the MLS $H_2O$ thresholds, however, we find relatively higher occurrence of 12.9%, 16.7%, 22.6%, and 14.9%. These differences can be considered a measure of the uncertainty of our calculations.

Note that we calculate a single threshold for the entire tropics, but different regions might have different thresholds. For example, the water vapor content over colder tropical western Pacific is lower (see Figure 3.2), meaning that the threshold there should probably be lower. However, with no consideration of continent-land differences, ocean convective cirrus clouds might be underestimated. Therefore, in our analysis the fractions over western Pacific region might be higher.

Overall, the two sets of thresholds result in the similar distribution patterns of cirrus clouds that are of convective origin. Since they are derived from different perspectives, we cannot evaluate which method is better or worse. But the fact that they generate approximately the similar thresholds supports they are both effective in determining cirrus that must come from convection.

4.2.2    Seasonal variations of convective cirrus

To examine the seasonal variations of the distribution of convective cirrus, we get thresholds associated with other seasons first.   Here we only derive T-Dependent thresholds.   Further verification from MLS observations is omitted here.   Based on previous section, the statistical effectiveness of the thresholds from both methods should be the same.

From Section 3, the theoretical maximum amount of $H_2O$ that air at critical temperature ($T_c$) reaches to saturation is defined as our T-Dependent threshold ($[H_2O(T_c)]_s$, in ppm).   Figure 4.5 shows the seasonal variations of $T_c$ and associated $[H_2O(T_c)]_s$ at different isentropic levels.   $T_c$ and $[H_2O(T_c)]_s$ are obtained at every 2.5 K with the range from 357 K to 410 K throughout the entire seasonal cycle.   The $T_c$ profiles show an apparent inversion from the lower TTL to the upper TTL, similar to the general variation of temperature profiles (due to the change of radiative heating rates), except here referring to temperatures from optically thin cirrus clouds.   At any specific isentropic level, the $T_c$ from high to low shows a trend from JJA, SON, MAM, to DJF, representing the general temperature trend from high to low as expected.   Thus, the associated $[H_2O(T_c)]_s$ decreases following the same pattern, i.e., the highest thresholds always show in JJA and the lowest always show in DJF.   An exception is noted at levels above 405 K where limited observations of cirrus cloud lead to less significant temperature analysis, statistically.   From the figure, thresholds during JJA appear to be the highest, mostly due to the Indian and South Asian monsoon effect, which brings a large amount of moisture into the air.
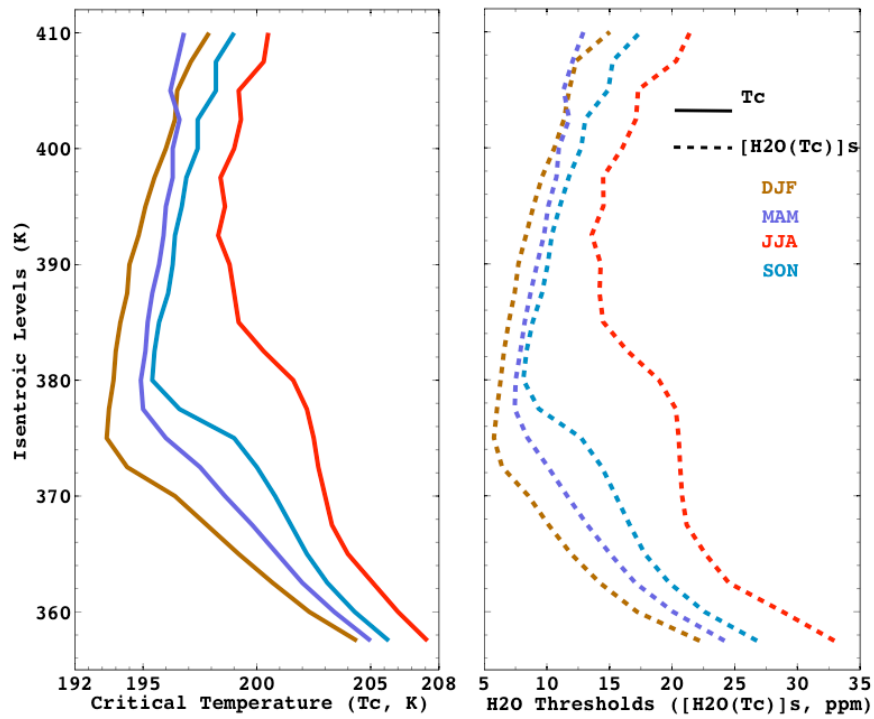
**Figure 4.5.** Seasonal variations of T-Dependent thresholds profiles. Critical temperature ($T_c$) in left panel and associated saturation volume mixing ratio $[H_2O(T_c)]_s$ are obtained at every 2.5 K from 357 K to 410 K through entire season cycle.

With thresholds of all seasons ready, we investigate the seasonal variations of convective cirrus. Figure 4.6 shows the seasonal fraction maps of convective cirrus occurrence identified by applying corresponding thresholds separately. The DJF maps are repeated from Figure 4.3. Regions of frequent convective cirrus are similar through all seasons. We see a clear modulation by Indian and South Asian monsoon during boreal summer, which drives the fraction maxima moving northward. Particularly over the western Pacific, a large-scale seasonal migration of convective cirrus clearly shows in

all isentropic levels. It shifts towards the north from DJF to JJA and then shifts back to the south.
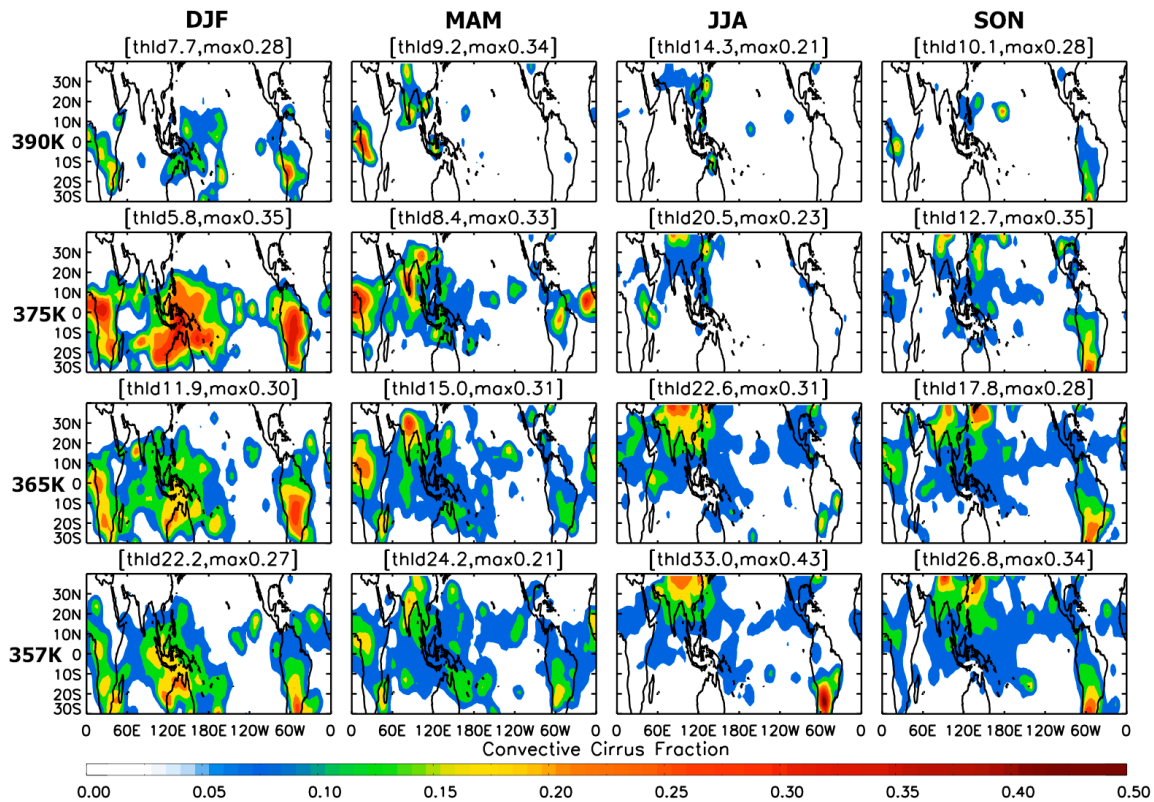


**Figure 4.6.** Seasonal map of convective cirrus fractions from 2008 December to 2009 November. The same, fractions are obtained on $4^o$x$2^o$ Lon-Lat grid boxes, and a 3-point smoothing has been applied to the grid box averages.

During JJA, we observe frequent occurrence of convective cirrus in the Tibetan Plateau at all levels due to the monsoon effects. This is expected because tropospheric convection, driven by elevated surface heating over Tibetan Plateau, usually develops deeper and reaches to higher altitudes during boreal summer [*Fu et al.*, 2006]. A similar

enhancement along the eastern coast of North America can be attributed to moist convection increasing during North American monsoon as well [*Weinstock et al.*, 2007].

Note that the frequency maps of convective cirrus depend on not only the occurrence of convective cirrus (the numerator) but also the occurrence of total cirrus clouds (the denominator) in each gridded averaging box. Therefore, the frequency values are highly dependent on the box sizes. But the general patterns should be consistent regardless of the size of the averaging boxes.

Table 4.2 summarizes the seasonal mean frequencies of occurrence of convective cirrus in the tropics. Unlike the tropical averages obtained for DJF, for seasonal variations we calculate averages around the entire tropics from 30$^{\circ}$S to 30$^{\circ}$N. At each isentropic level, convective cirrus occur more frequently during boreal winter and less frequently duing boreal summer, basically following the trend from DJF, MAM, SON, to JJA. One exception is at 390 K, where convective cirrus frequency is higher in JJA than in SON. This might be due to the small amount of thin cirrus observed at this level, which leads to uncertainty in the threshold, as we will discuss later.

**Table 4.2.** Seasonal fraction variations of convective cirrus around the tropics (30$^{\circ}$S to 30$^{\circ}$N) by applying the T-Dependent thresholds.

|        | DJF   | MAM   | JJA   | SON   |
|--------|-------|-------|-------|-------|
| 390 K  | 8.3%  | 8.1%  | 6.1%  | 5.6%  |
| 375 K  | 19.2% | 12.4% | 4.6%  | 6.5%  |
| 365 K  | 12.8% | 9.4%  | 7.7 % | 7.9%  |
| 357 K  | 10.9% | 8.9%  | 6.1%  | 7.7%  |

*Luo and Rossow* [2004] showed that at least half of the tropical cirrus are not directly related to convective detrainment. A study by *Rihimaki and McFarlane* [2010],

using 3 years of CALIPSO Cloud Layer data, revealed that 36% of cirrus clouds with base heights greater than 14 km are directly attached to optically thick clouds, by which they define as convective clouds. Apparently, we are getting lower frequencies than previous studies. This is because our thresholds produce a lower limit for the fraction of cirrus from convection. Those convective cirrus clouds that form with the amount of injected ice below our thresholds and those clouds that thinned out eventually cannot be identified by our thresholds.

## 4.3 Sensitivity analysis of the thresholds

In this section, we perform a sensitivity test to see how sensitive our results are to the threshold. For simplicity, we only perform the sensitivity test of CALIPSO T-Dependent method on boreal winter data. The results will show the same trend if we perform on the MLS $H_2O$ thresholds.

We applied +/- 20% variability of the thresholds to the three most enhanced regions marked in Figure 4.4 and the entire tropics at all levels to test their sensitivity to the final results. Figure 4.7 demonstrates the sensitivity of results to the changed thresholds. At all regions investigated, 375 K level has the most robust threshold due to the least variations when we changed the thresholds (cyan lines). At 375 K, when threshold changes from -20% to +20% to the original calculated values, the frequencies deviated relatively by +22% to -14%, +18% to -12%, +16% to -10%, and +21% to -11% for the box region over equatorial Africa, western Pacific, South America, and the entire tropics, respectively. For example, within the box marked in equatorial Africa, the original threshold is 5.8 ppm and the convective fraction is 23.2%. When we decrease

the original threshold by 20% to 4.6 ppm, the mean convective cirrus frequency increases by 22% to 28.3%; when we increase the thresholds by 20% to 7.0 ppm, the convective frequency decreases by 14% to 20.0%.

Figure 4.7 also shows that our results vary less at 365/375 K and more at 357/390 K with changed IWCs and thresholds. This is because 365 K and 375 K are well suited within the TTL, where our methods are designed to be qualified in identifying cirrus of convective origin. The 357 K is close to the TTL bottom where air features appear more likely to be troposphere, so our methods show relatively less effectiveness. The 390 K is the most sensitive to uncertainty in the threshold, especially over the box region in equatorial Africa, where the mean frequency of convective cirrus increases by 28% when threshold decreases by 20%. Meanwhile, when we increase threshold by 20%, the mean frequency decreases by 21%. Part of the reason may be attributed to the smaller amount of thin cirrus measurements in 390 K, which makes our results of critical temperature ($T_c$) statistically biased. Aware of the fact that our methods are based on statistical analysis of TTL air, the less effective ability of our methods due to limited data at 390 K are still tolerable.
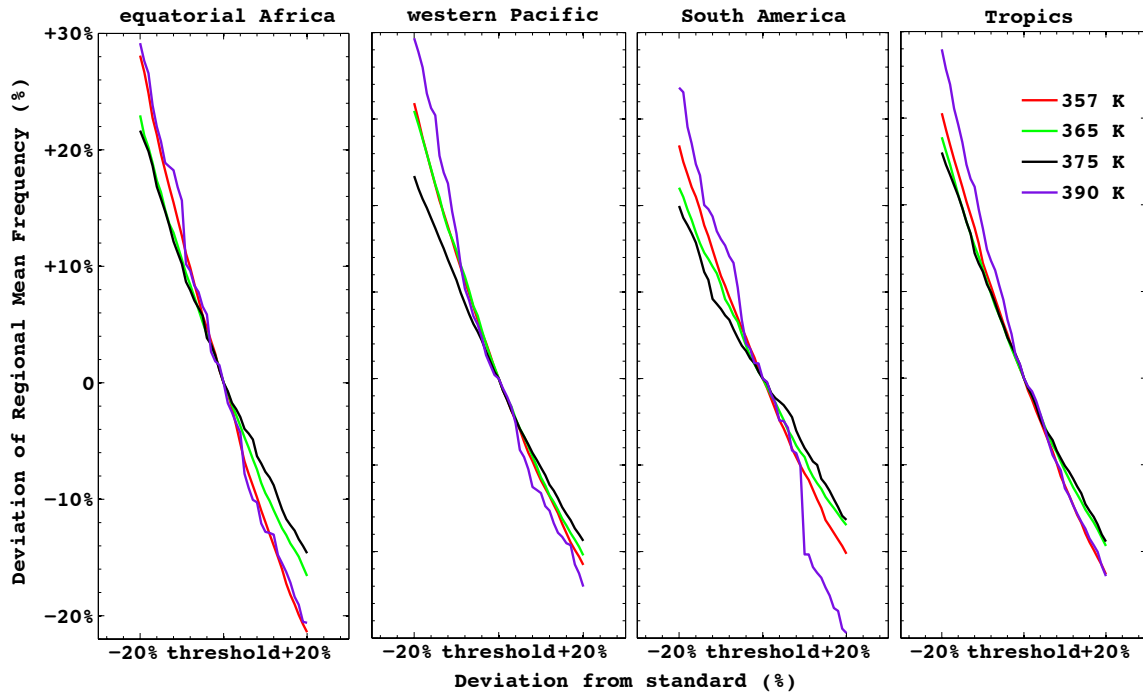
**Figure 4.7.** Sensitivity analysis of thresholds on three most enhanced regions of convective cirrus and the entire tropics.

We also found that when we applied the same variability on the threshold, either decrease 20% or increase about 20%, we see the final results deviated much more when thresholds are decreased. For example, when thresholds decrease about 20%, the prominent deviation from original results will tend to be 20-30%; when we increase the thresholds about the same extent to 20%, the deviation is just 10%-20%. This also shows that our thresholds are indeed the upper limits. Since they are already the highest value, increasing does not affect the final results too much.

## 4.4    Summary

In this section we examined the fractions of cirrus as well as that of convective cirrus. As expected, total cirrus and convective cirrus mainly occur in the three most

enhanced regions of convection: the tropical western Pacific, equatorial Africa, and northern South America. Applying the T-Dependent thresholds and MLS $H_2O$ thresholds reveal similar patterns of results. Within the TTL, convective cirrus occurs most frequently at 375 K, the classic level of tropical tropopause. Overall, convective cirrus occur more often in boreal winter and less in boreal summer. Performing the sensitivity test we found 375 K has the most reliable and robust thresholds and 390 K has the most uncertain ones.

# 5. SUMMARY AND FUTURE WORK

In this study we analyzed that in situ nucleation and convective anvil blow-off are responsible for TTL cirrus formation. Given that, for a cloud formed in situ, ice water content (IWC) cannot exceed the amount of water vapor ($H_2O$) available in the ambient air. We developed two methods to infer this amount of $H_2O$, which serves as our threshold. The first method yields the thresholds from direct observation of $H_2O$ in clear air by the MLS instrument, which we call the MLS $H_2O$ thresholds. The second method, using CALIPSO datasets, generates the threshold based on statistical analysis of the temperature of air in which in situ cirrus are found. We call it the T-Dependent thresholds. The thresholds from both methods match well, which builds our confidence in the methods we developed.

Applying the T-Dependent thresholds on CALIOP measurements from December 2008 to February 2009, we found that at least 20.1% of the tropical (considering 30°S-10°N) cirrus was definitively of convective origin at the tropopause (375 K). At lower levels, the TTL bottom (357K), and half way (365K) from bottom to the tropopause, at least 11.2% and 13.0% of cirrus must come from convective anvil detrainment in the same season, respectively. Above the tropopause at 390 K, we found only 8.5% were definitely of convective origin.

At each level, we found frequency maxima of occurring convective cirrus appear in three regions: western Pacific, equatorial Africa, and South America. The frequencies vary regionally with highest value seen in the Western Pacific (357 K and 375 K), Central Africa (390 K), or South America (365 K). See Table 4.1 for a review.

There is an obvious seasonal variation of occurrence of convective cirrus. Averaged over the entire tropics ($30^{o}$S to $30^{o}$N), we found convective cirrus occurs more frequently in boreal winter and less frequently in boreal summer, basically following the decreasing trend from DJF, MAM, SON, to JJA (Table 4.2). Our results show clear modulation by Asian summer monsoon and North American monsoon, which drives the maxima in total cirrus as well as in convective cirrus northward during boreal summer. This agrees well with many previous studies [e.g., *Massie et al.*, 2010].

Sensitivity tests show that the thresholds derived at 390 K have the largest uncertainty. This is because cirrus clouds occur less frequently at this height, and the limited observation results make our statistical results less significant. At lower levels, especially 375 K, our thresholds are robust.

Many previous studies have focused on the relationship between cirrus occurrence and deep convection. They compared cirrus observations with either outgoing longwave radiation (OLR, deep convection proxy) [*Massie et al.*, 2002] or convection observations from radar [*Sassen et al.*, 2009] to find the connection between them. Much of the previous results are consistent with ours, which adds confidence to our results.

It is important to recognize that our methods produce lower fractions of cirrus of convective origin because we are using the upper limits to identify convective cirrus. Besides, situations like 1) convective cirrus may be injected into the TTL with values of IWC below the threshold, and 2) the clouds could thin out with time and eventually reach IWC values below the threshold are not taken into consideration in our methods. Thus, the clouds that are not identified as convective cannot be assumed to have formed in situ. Instead, these clouds must be considered to have an uncertain origin.

For the next step in this research effort, we are planning to run a forward-trajectory model of the TTL to see if such a simple model can reproduce the observations. Comparisons of observations to the model will provide a fundamental test on the fidelity of the model simulations and a test of our understanding of the TTL. In particular, differences between observations and the model can be used to help us understand the shortcomings of models and give us insights into how air is processed in the TTL.

This model will provide insights to the roles that supersaturation and convection play in determining the occurrence patterns of TTL cirrus. This model estimates the location of in situ cirrus where relative humidity along the trajectory exceeds a specified threshold for condensation (100% for saturation or higher for supersaturation). When convective scheme is added, this model also predicts the convective cirrus. By varying the model parameters, we can see how that affects the locations of cirrus occurrence.

The results of the model's simulations of clouds can then be compared to the results we have obtained. We will also compare the model's prediction for TTL and lower stratospheric water vapor to MLS measurements to make sure that these are reasonable.

**REFERENCES**

Alcala, C. M., and A. E. Dessler (2002), Observations of deep convection in the tropics using the Tropical Rainfall Measuring Mission (TRMM) precipitation radar, *J. Geophys. Res.*, 107(D24), 4792, doi:10.1029/2002JD002457.

Bluestein, H.B. (1992): Principles of Kinematics and Dynamics. Vol. I. *Synoptic– Dynamic Meteorology in Midlatitudes*, pp. 23, Oxford Univ. Press.

Boehm, M., and J. Verlinde (2000), Stratospheric influence on upper tropospheric tropical cirrus, *Geophys. Res. Lett.*, 27(19), 3209–3212.

Boehm, M. T., and S. Lee (2003), The implications of tropical Rossby waves for tropical tropopause cirrus formation and for the equatorial upwelling of the Brewer-Dobson circulation, *J. Amos. Sci.*, 60, 247 – 261.

Brewer, A. W. (1949), Evidence for a world circulation provided by the measurements of helium and water vapor distribution in the stratosphere, *Quart. J. Royal. Met. Soc.*, 75, 351–363.

Churchill, D. D., and R. A. Houze, Jr. (1990), Radiatively driven stratosphere-troposphere interactions near the tops of tropical cloud clusters, Preprint Volume, *7th Conf. on Atmos. Radiation*, San Francisco, Calif., J125-J128.

Comstock, J. M., T. P. Ackerman, and G. G. Mace (2002), Ground-based lidar and radar remote sensing of tropical cirrus clouds at Nauru Island: Cloud statistics and radiative impacts, *J. Geophys. Res.*, 107(D23), 4714, doi:10.1029/2002JD002203.

Comstock, J. M., and C. Jakob (2004), Evaluation of tropical cirrus cloud properties derived from ECMWF model output and ground based measurements over Nauru Island, *Geophys. Res. Lett.*, *31*, L10106, doi:10.1029/2004GL019539.

Danielsen, E. F. (1993), In situ evidence of rapid, vertical, irreversible transport of lower tropospheric air into the lower tropical stratosphere by convective cloud turrets and by larger-scale upwelling in tropical cyclones, *J. Geophys. Res.*, *98*(D5), 8665–8681, doi:10.1029/92JD02954.

Dessler, A. E., S. P. Palm, W. D. Hart, and J. D. Spinhirne (2006), Tropopause-level thin cirrus coverage revealed by ICESat/Geoscience Laser Altimeter System, *J. Geophys. Res.*, 111, D08203, doi:10.1029/2005JD006586.

Dessler, A. E., and K. Minschwaner (2007), An analysis of the regulation of tropical tropospheric water vapor, J. Geophys. Res., 112, D10120, doi: 10.1029/2006JD007683.

Dinh, T. P., D. R. Durran, and T. P. Ackerman (2010), Maintenance of tropical tropopause layer cirrus, *J. Geophys. Res.*, 115, D02104, doi:10.1029/2009JD012735.

Eguchi, N., T. Yokota, and G. Inoue (2007), Characteristics of cirrus clouds from ICESat/GLAS observations, *Geophys. Res. Lett.*, 34, L09810, doi:10.1029/2007GL029529.

Evans, S.J., R. Toumi, J.E. Harries, M.P. Chipperfield and J.M. Russel (1998), Trends in stratospheric humidity and the sensitivity of ozone to these trends, *J. Geophys. Res.*, 103, pp. 8715–8725.

Folkins, I., M. Loewenstein, J. Podolske, S. J. Oltmans, and M. Proffitt (1999), A barrier to vertical mixing at 14 km in the tropics: Evidence from ozonesondes and aircraft

measurements, *J. Geophys. Res.*, 104(D18), 22,095–22,102, doi:10.1029/1999JD900404.

Forster, P. M. F., and K. P. Shine (1999), Stratospheric water vapor changes as a possible contributor to observed stratospheric cooling, *Geophys. Res. Lett.*, 26, 3309–3312.

Fu, Q., Y. Hu, and Q. Yang (2007), Identifying the top of the tropical tropopause layer from vertical mass flux analysis and CALIPSO lidar cloud observations, *Geophys. Res. Lett.*, 34, L14813, doi:10.1029/2007GL030099.

Fu, R., Y. Hu, J. S. Wright, J. H. Jiang, R. E. Dickinson, M. Chen, M. Filipiak, W. G. Read, J. W. Wa ters, and D. L. Wu (2006), Short circuit of water vapor and polluted air to the global stratosphere by convective transport over the Tibetan Pla teau. Proc. *Natl. Acad. Sci.* , 103, 5664–5669.

Fueglistaler, S., A. E. Dessler, T. J. Dunkerton, I. Folkins, Q. Fu, and P. W. Mote (2009), Tropical tropopause layer, *Rev. Geophys.*, 47, RG1004, doi:10.1029/2008RG000267.

Fujiwara, M., S. Iwasaki, A. Shimizu, Y. Inai, M. Shiotani, et al. (2009), Cirrus observations in the tropical tropopause layer over the western Pacific, *J. Geophys. Res.*, *114*, D09304, doi:10.1029/2008JD011040.

Gettelman, A., W. J. Randel, F. Wu, and S. T. Massie (2002), Transport of water vapor in the tropical tropopause layer, *Geophys. Res. Lett.*, *29*(1), 1009, doi:10.1029/2001GL013818.

Gettelman, A., P. M. de F. Forster, M. Fujiwara, Q. Fu, H. Vömel, L. K. Gohar, C. Johanson, and M. Ammerman (2004), Radiation balance of the tropical tropopause layer, *J. Geophys. Res.*, 109, D07103, doi:10.1029/2003JD004190.

Haladay, T., and G. Stephens (2009), Characteristics of tropical thin cirrus clouds
deduced from joint CloudSat and CALIPSO observations, *J. Geophys. Res.*, 114,
D00A25, doi:10.1029/2008JD010675.

Heymsfield, A. J., and L. J. Jahnsen, (1974): Microstructure of tropopause cirrus layers,
in *Proceedings of the Sixth Conference on Aerospace and Aeronautical
Meteorology*, El Paso, TX, pp. 43–48, *Am. Meteorol. Soc.*, Boston, Mass.

Heymsfield, A. J., D. Winker, and G.-J. van Zadelhoff, (2005): Extinction-ice water
content-effective radius algorithms for CALIPSO. *Geophys. Res. Lett.*, 32, L10807,
doi:10.1029/2005GL022742.

Highwood, E.J. and B.J. Hoskins (1998), The tropical tropopause. *Quart. J. Royal. Met.
Soc.*, 124, 1579-1604.

Holton, J. R., and A. Gettelman (2001), Horizontal transport and the dehydration of the
stratosphere, *Geophys. Res. Lett.*, 28, 2799–2802, doi:10.1029/2001GL01314.

Hu, Y. and and Coauthors. (2009), CALIPSO/CALIOP Cloud Phase Discrimination
Algorithm, *J. Atmos. Oceanic Technol.*, 26, pp. 2293-2309.

Hu, Y., D. Winker, M. Vaughan, B. Lin, A. Omar, et al. (2009), CALIPSO/CALIOP
cloud phase discrimination algorithm. *J. Atmos. Ocean. Technol.*, *26*, 2206–2309.

Hurst, D. F., S. J. Oltmans, H. Vömel, K. H. Rosenlof, S. M. Davis, E. A. Ray, E. G.
Hall, and A. F. Jordan (2011),Stratospheric water vapor trends over Boulder,
Colorado: Analysis of the 30 year Boulder record, *J. Geophys. Res.*, 116, D02306,
doi:10.1029/2010JD015065.

Immler, F., Treffeisen, R., Engelbart, D., Krüger ,K., and Schrems, O. (2008), Cirrus,

contrails and ice supersaturated regions in high pressure systems at northern mid

latitudes, *Atmos. Chem. Phys.*, 8. 1689-1699.

Jarnot, R. F., V. S. Perun, and M. J. Schwartz (2006), Radiometric and spectral

performance and calibration of the GHz bands of EOS MLS, *IEEE Trans. Geosci.

Remote Sens.*, 44, 1131–1143.

Jensen, E., O. Toon, H. Selkirk, J. Spinhirne, and M. Schoeberl (1996), On the formation

and persistence of subvisible cirrus clouds near the tropical tropopause, *J. Geophys.

Res.*, 101(D16), 21,361–21,37.

Jiang, J. H., et al. (2010), Five year (2004–2009) observations of upper tropospheric

water vapor and cloud ice from MLS and comparisons with GEOS-5 analyses, *J.

Geophys. Res.*, 115, D15103, doi:10.1029/2009JD013256.

Liou, K. N. (1986), Influence of cirrus clouds on weather and climate processes: a global

perspective. *Mon. Weather. Rev*. 114, 1167-1199.

Liu, Z., Kuehn, R., Vaughan, M., Winker, D., Omar, A., Powell, K., Trepte, C., Hu, Y.,

and Hostetler, C. (2010): The CALIPSO Cloud And Aerosol Discrimination:

Version 3 Algorithm and Test Results, available at:

http://webcache.googleusercontent.com/search?q=cache:o24s5FFWjI0J:eosweb.larc.

nasa.gov/PRODOCS/calipso/Quality_Summaries/CALIOP_L2ProfileProducts_3.01.

html+The+CALIPSO+Cloud+And+Aerosol+Discrimination:+Version+3+Algorithm

+and+Test+Results&cd=2&hl=en&ct=clnk&gl=us&source=www.google.com).

Livesey, N. J., W. V. Snyder, W. G. Read, and P. A. Wagner (2006), Retrieval algorithms for the EOS Microwave Limb Sounder (MLS), *IEEE Trans. Geosci. Remote Sens.*, 44, 1144–1155.

Livesey, N. J., W. G. Read, A. Lambert, R. E. Cofield, D. T. Cuddy, et al. (2007), EOS MLS version 2.2 Level 2 data quality and description document, *Tech. Rep.* JPL. D-33509, Jet Propul. Lab, Pasadena, Calif.

Luo, Z., and W.B. Rossow, 2004: Characterizing tropical cirrus life cycle, evolution, and interaction with upper-tropospheric water vapor using Lagrangian trajectory analysis of satellite observations. *J. Climate*, 17, 4541-4563, doi:10.1175/3222.1.

Lynch, D. K., K. Sassen, D. O. Starr, and G. Stephens, Eds. (2002), Cirrus. Oxford University Press, 480 pp.

Mace, G. G., M. Deng, B. Soden, and E. Zipser (2006), Association of tropical cirrus in the 10–15-km layer with deep convective sources: An observational study combining millimeter radar data and satellite-derived trajectories, *J. Atmos. Sci.*, 63, 480–503.

Massie, S., A. Gettelman, W. Randel, and D. Baumgardner (2002), Distribution of tropical cirrus in relation to convection, *J. Geophys. Res.*, 107(D21), 4591, doi:10.1029/2001JD001293.

Massie, S., W. Randel, F. Wu, D. Baumgardner, and M. Hervig (2003), Halogen Occultation Experiment and Stratospheric Aerosol and Gas Experiment II observations of tropopause cirrus and aerosol during the 1990s, *J. Geophys. Res.*, 108(D7), 4222, doi:10.1029/2002JD002662.

Massie, S. T., J. Gille, C. Craig, R. Khosravi, J. Barnett, W. Read, and D. Winker (2010), HIRDLS and CALIPSO observations of tropical cirrus, *J. Geophys. Res.*, 115, D00H11, doi:10.1029/2009JD012100.

McFarquhar, G., A. Heymsfield, J. Spinhirne, and B. Hart (2000), Thin and subvisual tropopause tropical cirrus: Observations and radiative impacts, *J. Atmos. Sci.*, 57(12), 1841–1853.

Mergenthaler, J. L., A. E. Roche, J. B. Kumer, and G. A. Ely (1999), Cryogenic Limb Array Etalon Spectrometer observations of tropical cirrus, *J. Geophys. Res.*, 104(D18), 22,183–22,194, doi:10.1029/1999JD900397.

Murphy, D. M. and T. Koop (2005), Review of the vapour pressures of ice and supercooled water for atmospheric applications, *Quart. J. Royal. Met. Soc.*, 131, 1539-1565.

Nazaryan, H., M. P. McCormick, and W. P. Menzel (2008), Global characterization of cirrus clouds using CALIPSO data, *J. Geophys. Res.*, 113, D16211, doi:10.1029/2007JD009481.

Oldmans, S.J. and Hofmann, D.J. (1995), Increase in lower stratospheric water vapour and a midlatitude northern hemisphere site from 1981–1994, *Nature*, 374, pp. 146–149.

Pfister, L., H. B. Selkirk, E.J. Jensen, M. R. Schoeberl, O. B. Toon, et al. (2001), Aircraft observations of thin cirrus clouds near the tropical tropopause, *J. Geophys. Res.*, 106(D9), 9765–9786.

Prabhakara, C., R.S. Fraser, G. Dalu, M.C. Wu and R.J. Curran (1988), Thin cirrus clouds: seasonal distribution over oceans deduced from Nimbus-4 IRIS, *J. Appl. Meteor.* 27, pp. 379–399.

Prabhakara, C., Kratz, D.P., Yoo, J.M., Dalu, G., Vernerkar, A. (1993), Optically thin cirrus clouds radiative impact on the warm pool, *J. Quant. Spectrosc. Radiat. Transfer*, 49, 467–483.

Protat, A., J. Delanoë, D. Bouniol, A. J. Heymsfield, A. Bansemer, P. Brown (2007), Evaluation of Ice Water Content Retrievals from Cloud Radar Reflectivity and Temperature Using a Large Airborne In Situ Microphysical Database. *J. Appl. Meteor. Climatol.*, 46, 557–572. doi: 10.1175/JAM2488.1.

Read, W. G., et al. (2007), Aura Microwave Limb Sounder upper tropospheric and lower stratospheric $H_2O$ and relative humidity with respect to ice validation, *J. Geophys. Res.*, 112, D24S35, doi:10.1029/2007JD008752.

Reed, R. J., and C. L. Vlcek (1969), The annual temperature variation in the lower tropical stratosphere, *J. Amtos. Sci.*, 26, 163–167.

Rienecker, M. M., et al. (2008), The GEOS-5 data assimilation system—Documentation of versions 5.0.1, 5.1.0, and 5.2.0, *NASA Tech. Memo., TM–2008–104606*, vol. 27, 97 pp.

Riihimaki, L. D., and S. A. McFarlane (2010), Frequency and morphology of tropical tropopause layer cirrus from CALIPSO observations: Are isolated cirrus different from those connected to deep convection?, *J. Geophys. Res.*, 115, D18201, doi:10.1029/2009JD013133.

Rosenfield, J. E., D. B. Considine, M. R. Schoeberl, and E. V. Browell (1998), The

impact of subvisible cirrus clouds near the tropical tropopause on stratospheric water

vapor, *Geophys. Res. Lett.*, 25(11), 1883–1886, doi:10.1029/98GL01294.

Rosenlof, K. H., et al. (2001), Stratospheric water vapor increases over the past half-

century, *Geophys. Res. Lett.*, 28(7), 1195–1198, doi:10.1029/2000GL012502.

Rossow, W.B., and Schiffer, R.A. (1999): Advances in Understanding Clouds from

ISCCP. *Bull. Amer. Meteor. Soc.*, 80, 2261-2288.

Sassen, K., and B. S. Cho (1992): Subvisual-thin cirrus lidar dataset for satellite

verification and climatological research. *J. Appl. Meteor.,* 31, 1275–1285.

Sassen, K., and G. G. Mace (2002), Ground based remote sensing of cirrus clouds, in

Cirrus, edited by D. Lynch et al., pp. 168–195, Oxford Univ. Press, New York.

Sassen, K., Z. Wang, and D. Liu (2008), Global distribution of cirrus clouds from

CloudSat/Cloud-Aerosol Lidar and Infrared Pathfinder Satellite Observations

(CALIPSO) measurements, *J. Geophys. Res.*, 113, D00A12,

doi:10.1029/2008JD009972, [printed 114(D8), 2009].

Sassen, K., Z. Wang, and D. Liu (2009), Cirrus clouds and deep convection in the tropics:

Insights from CALIPSO and CloudSat, *J. Geophys. Res.*, 114, D00H06,

doi:10.1029/2009JD011916.

Schwartz, M. J., et al. (2008), Validation of the Aura Microwave Limb Sounder

temperature and geopotential height measurements, *J. Geophys. Res.*, 113, D15S11,

doi:10.1029/2007JD008783.

Schwartz, M. C., and G. G. Mace (2010), Co-occurrence statistics of tropical tropopause layer cirrus with lower cloud layers as derived from CloudSat and CALIPSO data, *J. Geophys. Res.*, 115, D20215, doi:10.1029/2009JD012778.

Sherwood, S.C., and A.E. Dessler (2000), On the control of stratospheric humidity. *Geophys. Res. Lett.*, 27, 2513-2516.

Sherwood, Steven C., Andrew E. Dessler (2001), A Model for Transport across the Tropical Tropopause. *J. Atmos. Sci.*, 58, 765–779.

Smith, C. A., J. D. Haigh, and R. Tuomi (2001), Radiative forcing due to trends in stratospheric water vapor, *Geophys. Res. Lett.*, 28, 179–182.

Solomon, S. C., et al. (2010), Contributions of Stratospheric Water Vapor to Decadal Changes in the Rate of Global Warming, *Science*, 327, 1219. DOI: 10.1126/science.1182488.

Stephens, G. L., Vane, D. G., Boain, R. J., Mace, G. G., Sassen, K., Wang, Z., Illingworth, A. J., O'Connor, E. J., Rossow, W. B., Durden, S. L., Miller, S. D., Austin, R. T., Benedetti, A., Mitrescu, C., and the CloudSat Science Team (2002), The CloudSat mission and the A-train, *B. Am. Meteor. Soc.*, 83, 1771–1790, 2002.

Wang, P.-H., McCormick, M.P., Poole, L.R., Chu, W.P., Yue, G.K., Kent, G.S. and Skeens, K.M. (1994), Tropical high cloud characteristics derived from SAGE II extinction measurements. *Atmos. Res.*, 34, pp. 53–83.

Wang, P., P. Minnis, M. McCormick, G. Kent, and K. Skeens (1996), A 6-year climatology of cloud occurrence frequency from Stratospheric Aerosol and Gas Experiment II observations (1985-1990), *J. Geophys. Res.*, 101(D23), 29,407–29,429.

Waters, J. W., et al. (2006), The Earth Observing System Microwave Limb Sounder (EOS MLS) on the Aura satellite, *IEEE Trans. Geosci. Remote Sens.*, 44, 1075–1092, doi:10.1109/TGRS.2006.873771.

Weinstock, E. M., et al. (2007), Quantifying the impact of the North American monsoon and deep midlatitude convection on the subtropical lowermost stratosphere using in situ measurements, *J. Geophys. Res.*, 112, D18310, doi:10.1029/2007JD008554.

Winker, D., and C. Trepte (1998), Laminar cirrus observed near the tropical tropopause by LITE, *Geophys. Res. Lett.*, 25(17), 3351–3354.

Winker, D. M., Pelon, J., and McCormick, M. P. (2003), The CALIPSO mission: Spaceborne lidar for observation of aerosols and clouds, Proc. SPIE, 4893, 1–11. doi:10.1117/12.466539.

Wu, D. L., J. H. Jiang, W. G. Read, R. T. Austin, C. P. Davis, A. Lambert, G. L. Stephens, D. G. Vane, and J. W. Waters (2008), Validation of the Aura MLS cloud ice water content measurements, *J. Geophys. Res.*, 113, D15S10, doi:10.1029/2007JD008931.

Wu, D. L., et al. (2009), Comparisons of global cloud ice from MLS, CloudSat, and correlative data sets, *J. Geophys. Res.*, *114*, D00A24, doi:10.1029/2008JD009946.

Young, S. A., andM. A. Vaughan, 2009: The retrieval of profiles of particulate extinction from Cloud Aerosol Lidar Infrared Pathfinder Satellite Observations (CALIPSO) data: Algorithm description. *J. Atmos. Oceanic Technol.*, 26, 1105–1119.

**APPENDIX**

1. About the new ice saturation relation from Murphy and Koop (2005).

Using new laboratory data on the molar heat capacity of supercooled water as constraints, *Murphy and Koop* [2005] formulated a new expression for the vapor pressure over (hexagonal) ice, which presents a much better fit than previous formulations. The new relation is as following

$e_{si}$ = *exp(9.550426 – 5723.265/T + 3.53068 ln(T) – 0.00728332 T)*   (in *Pa*)

This formula is suitable for saturation vapor pressure with respect to ice of temperatures below -80°C.

2. Converting IWC from mg/m$^3$ to volume mixing ratio in parts per million (ppmv).

$$[IWC(ppmv)] = \frac{IWC(mg/m^3) \times \dfrac{1g}{1000mg} / 18.016(g/mol)}{\dfrac{Pres(hPa) \times \dfrac{100Pa}{1hPa}}{8.314(J/(mol \cdot K)) \times Temp(K)}} \times 10^6$$

**VITA**

Tao Wang received his Bachelor of Science degree in atmospheric sciences at Yunnan University in Kunming, China, on July 2003. Then he started working at the Cold and Arid Regions of Environment and Engineering Institute, Chinese Academy of Sciences, as a research assistant since August 2003. In September 2009, he started his study in the Department of Atmospheric Sciences at Texas A&M University, and received his Master of Science degree in May 2011.

Mr. Wang will continue his studies in the Department of Atmospheric Sciences at Texas A&M University beginning in May 2011. He may be reached at the Department of Atmospheric Sciences, Texas A&M University, 3150 TAMU, College Station, TX, 77843. His email address is tao.wang@tamu.edu.

**Publications**

Wu, T., W. Dong, Y. Zhang, and T. Wang (2011), Comparison of positive and negative compact intracloud discharges, *J. Geophys. Res.*, *116*, D03111, doi:10.1029/2010JD015233.